HHS Public Access

Author manuscript

Cell. Author manuscript; available in PMC 2021 January 09.

Published in final edited form as:

Cell. 2020 January 09; 180(1): 122–134.e10. doi:10.1016/j.cell.2019.11.041.

Structure of the Cardiac Sodium Channel

Daohua Jiang[†,1], **Hui Shi**[†,1,4], **Lige Tonggu**[1], **Tamer M. Gamal El-Din**[1], **Michael J. Lenaeus**[1,2], **Yan Zhao**[3], **Craig Yoshiaki**[3], **Ning Zheng**[*,1,4], **William A. Catterall**[*,1,5]

[1]Department of Pharmacology, University of Washington, Seattle, WA 98195, USA

[2]Division of General Internal Medicine, Department of Medicine, University of Washington, Seattle, WA 98195, USA

[3]Vollum Institute, Oregon Health & Science University, Portland, OR 97239, USA

[4]Howard Hughes Medical Institute, University of Washington, Seattle, WA 98195, USA

[5]Lead contact

SUMMARY

Voltage-gated sodium channel $Na_v1.5$ generates cardiac action potentials and initiates the heartbeat. Here we report structures of $Na_V1.5$ at 3.2–3.5 Å resolution. $Na_V1.5$ is distinguished from other sodium channels by a unique glycosyl moiety and loss of disulfide-bonding capability at the $Na_V\beta$ subunit-interaction sites. The antiarrhythmic drug flecainide specifically targets the central cavity of the pore. The voltage sensors are partially activated, and the fast-inactivation gate is partially closed. Activation of the voltage sensor of Domain III allows binding of the IFM motif to the inactivation-gate receptor. Asp and Ala in the selectivity motif DEKA line the walls of the ion-selectivity filter, whereas Glu and Lys are in positions to accept and release Na^+ ions via a charge-delocalization network. Arrhythmia mutation sites undergo large translocations during gating, providing a potential mechanism for pathogenic effects. Our results provide detailed insights into $Na_v1.5$ structure, pharmacology, activation, inactivation, ion selectivity, and arrhythmias.

In Brief

The high-resolution structure of the cardiac sodium channel gives detailed insights into voltage-dependent activation, ion selectivity, arrhythmia mechanisms, and antiarrhythmic drug action at the atomic level.

[*]Correspondence: nzheng@uw.edu and wcatt@uw.edu.
[†]These authors contributed equally: Daohua Jiang, and Hui Shi

Author Contributions

D.J., T.M.G., M.J.L., N.Z., and W.A.C. designed the experiments, D.J., H.S., L.T., T.M.G., C.Y., and Y.Z. carried out the experiments, all authors analyzed and interpreted the results, D.J., N.Z., and W.A.C. wrote the paper, and all authors reviewed and revised the paper.

Declaration of interests

The authors declare no competing interests.

Graphical Abstract

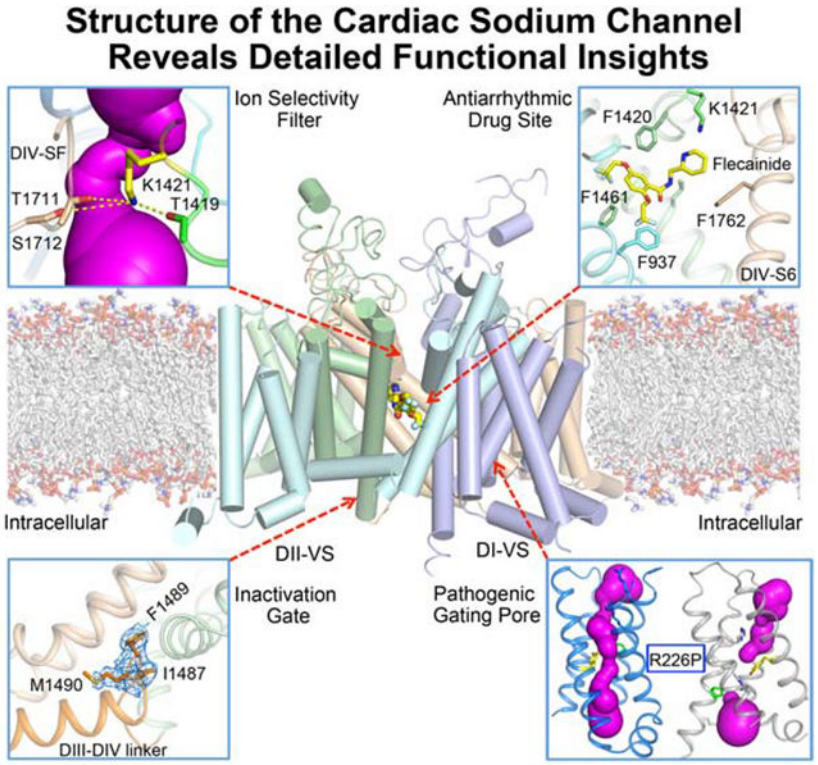

INTRODUCTION

Cardiac sodium channels generate the up-stroke of the cardiac action potential by activating rapidly in response to membrane depolarization and conducting Na^+ inward across the membrane (Catterall and Maier, 2015). The rate of rise of the action potential, which depends on rapid activation of voltage-gated sodium channels, controls the rate and homogeneity of propagation of the action potential through cardiac tissue (Catterall and Maier, 2015). Voltage-gated sodium channel 1.5 ($Na_V1.5$) is the predominant sodium channel expressed in myocardial cells (Fozzard and Hanck, 1996; Rogart et al., 1989). Dysfunction of $Na_V1.5$ owing to mutations or pathophysiological conditions causes life-threatening cardiac arrhythmias (Liu et al., 2003b), which are terminated and prevented by treatment with antiarrhythmic drugs (Sampson and Kass, 2011). Although other voltage-gated sodium channels are expressed in the heart, they are unable to compensate for dysfunction of $Na_V1.5$, which highlights the importance of this sodium channel in cardiac physiology and pathophysiology.

Voltage-gated sodium channels in eukaryotes consist of a high molecular weight pore-forming α-subunit of approximately 2000 amino acid residues containing four homologous domains (*D*I-*D*IV) (Catterall, 2000; Noda et al., 1984). Each domain of the α-subunit is composed of six transmembrane helices organized in two functional modules. The first four segments (S1-S4) form the voltage-sensing module (VS), whereas the last 2 segments (S5-S6) and a P-loop between them form the pore module (PM). The VS and PM are connected

by the α-helical S4-S5 linker. The intracellular linker connecting *D*III and *D*IV serves as the fast inactivation gate, which closes the pore within 1–2 msec after opening. In contrast, prokaryotic sodium channels are composed of four identical subunits, which are similar in structure to one domain of the eukaryotic α-subunits, and there is no structural equivalent of the fast inactivation gate (Payandeh et al., 2011; Ren et al., 2001).

Most eukaryotic sodium channels contain one or two auxiliary β-subunits (Isom et al., 1994; O'Malley and Isom, 2015). β1 and β3 bind to the α-subunit by noncovalent interactions, whereas β2 and β4 are linked by a disulfide bond. The β-subunits are composed of an extracellular Ig-like domain and a single transmembrane segment. They regulate channel voltage dependence, gating kinetics, cell-surface localization, and density.

High-resolution crystal structures of bacterial sodium channels and cryo-electron microscopic (cryo-EM) structures of eukaryotic sodium channels from nerve and skeletal muscle reveal similar architectures (Catterall et al., 2017; Pan et al., 2019; Pan et al., 2018; Payandeh et al., 2011; Shen et al., 2019). The central pore is formed by the PMs of the four subunits or domains. The four VS are positioned on the periphery of the PM in approximately square symmetry, and they are activated in these structures, placing the S4 segment containing the gating charges in an outward position. We used voltage-shifting mutations and disulfide crosslinking to trap the resting state of the bacterial sodium channel Na_VAb at 0 mV and determined its structure by cryo-EM (Wisedchaisri et al., 2019). Major changes in the conformation of the VS, the S4-S5 linker, and the intracellular activation gate were observed. These studies have given important insights into the structure and function of sodium channels

To discover the key structural features of $Na_V1.5$ and relate them to the structural basis for its physiological function and its dysfunction in cardiac arrhythmias, we have determined the cryo-EM structure of the rat $Na_v1.5$ α-subunit at 3.2–3.5 Å resolution. Our experiments provide a blueprint for understanding cardiac sodium channel structure, pharmacology, activation, inactivation, sodium selectivity, and disease mutations.

RESULTS AND DISCUSSION

Structure Determination of $Na_v1.5$ by CryoEM

$Na_V1.5$ is composed of approximately 2000 amino acid residues with large intracellular N- and C-termini and large intracellular segments that connect the four domains (Catterall et al., 2017; Fozzard and Hanck, 1996; Rogart et al., 1989). These intracellular segments, which are predicted to be structurally flexible, were not observed in previous cryo-EM structures of sodium channels (Pan et al., 2018; Shen et al., 2019; Shen et al., 2017). In order to optimize expression and homogeneity of rat $Na_v1.5$, constructs with truncated N- and C-termini and shortened interdomain linkers were screened by expression as fusion proteins with GFP and Fluorescence-detection Size Exclusion Chromatography (FSEC) (Goehring et al., 2014). Constructs were selected that have combined truncations and deletions, improved homogeneity and expression, and high voltage-activated Na^+ conductance. One of these $Na_V1.5$ constructs with deletions in *D*I-*D*II (Leu462-Gly658), *D*II-*D*III (Ser1069-Pro1189),

and the C-terminus (Leu1898-Val2019) was selected for further electrophysiological and structural studies.

This well-structured core transmembrane construct of rat $Na_V1.5$ ($rNa_v1.5_C$) was expressed in human embryonic kidney (HEK) cells and analyzed by whole-cell voltage clamp (see Star Methods and (Yarov-Yarovoy et al., 2012)). These recordings revealed typical inward sodium currents in response to depolarizing stimuli (Figure S1A). Proteolytic cleavage of cytoplasmic loops shifts activation curves of mammalian sodium channels negatively (Bennett, 2001). Likewise, we found that $rNa_v1.5_C$ has a substantial negative shift in the voltage dependence of activation (−50 mV) compared to native rat $Na_v1.5$, suggesting that activated/inactivated states are favored (Figure S1A).

$rNa_v1.5_C$ was expressed at high levels in the cell line HEK293S GnTI$^-$, which limits N-linked glycosylation (Reeves et al., 2002). After solubilization, affinity purification, and two rounds of size-exclusion chromatography, a peak of protein containing only the 230-kDa $rNa_V1.5_C$ α subunit was collected for structural studies (Figure S1D, E). Detailed descriptions of protein expression, purification, cryo-EM imaging, and data processing are presented in Star Methods.

We imaged $rNa_v1.5_C$ by cryo-EM (Figure S1F, G; Figure S2A) and constructed a 3D map to an overall resolution of 3.5 Å (Figure 1A), based on the gold standard Fourier shell correlation criterion (Figure S2B–D) (Henderson et al., 2012). The PM in the center of the structure has higher resolution, approaching 3.3 Å, while the four VS have slightly lower resolution (Figure S2B). The high-quality electron density map allowed us to build an atomic model for $rNa_v1.5_C$ containing *D*I (missing a short extracellular loop Ala298-Asn303), *D*II (missing the sequence Leu799-Leu805 between S3 and S4), *D*III, *D*IV, and the *D*III-*D*IV linker (Figure 1A–D, Figure S3). We observed weak electron density on the intracellular side of *D*I-VS representing the N-terminus (Figure 1A). In a different protein sample prepared with 0.5 mM flecainide, the resolution of the $rNa_v1.5_C$-flecainide complex was improved to 3.24 Å (Figure 2A; Figures S4–S6). No electron density was found for loops between *D*I and *D*II, *D*II and *D*III, or the CTD containing the EF-hand like domain, suggesting that these segments are disordered or mobile.

Similar to other sodium channel structures, the four domains are assembled in a domain-swapped arrangement (Figure 1B). The structure of $rNa_v1.5_C$ can be superimposed well with the human $Na_v1.7$ α-subunit (Shen et al., 2019) with R.M.S.D of 1.3 Å over 1153 Cα atoms in the core region, consistent with high sequence similarity (75.5% identity). The transmembrane region also overlays well with the bacterial sodium channel Na_VAb (Cα R.M.S.D of 3.2 Å for *D*I) (Payandeh et al., 2011), illustrating the strong structural conservation of the VS and PM in sodium channels from bacteria to man. Strong electron density is observed for five Asn-linked glycosylation sites and 16 lipid or detergent molecules (Figure 1B, Figure S3E, F). Three of these specifically bound lipid molecules are also observed in $Na_V1.4$ (Pan et al., 2018), and two are conserved in Na_VAb as well (Payandeh et al., 2011), highlighting the potential functional significance of these conserved lipid moieties and their binding sites.

Altered Interaction Sites for $Na_V\beta$ Subunits

Despite high overall similarity with other sodium channels, there are key differences in the binding sites for the auxiliary $Na_V\beta$-subunits in $rNa_v1.5_C$. In contrast to sodium channels from brain and skeletal muscle, no β subunits were observed in biochemical studies of cardiac sodium channels (Gordon et al., 1988; Lombet and Lazdunski, 1984), and co-expression of the β-subunit increases expression but does not modulate the kinetics or voltage dependence of $Na_V1.5$ (Makita et al., 1994; Qu et al., 1995). In our hands, co-expressed $Na_V\beta1$ and $Na_V\beta2$ do not stably associate with $Na_V1.5$. These studies indicate that $Na_V\beta$-subunits do not interact with $Na_V1.5$ as strongly as with sodium channels in nerve and skeletal muscle. In comparison to $Na_V1.7$, (Figure 1C, D, magenta), we found unexpectedly that Asn319 has unambiguous density for an N-linked carbohydrate moiety, which would clash with β-sheet 2 and β-sheet 3 of the Ig-like domain of the p1-subunit for its binding to the $Na_v1.7$ (Figure 1E, upper panel; Figure S3F). The amino acid sequence near Asn319 (Asn-Gly-Thr) encodes a typical core N-linked glycosylation site. Sequence alignment of Asn319 indicates that it is a unique glycosylation site among Na_v channels ($Na_v1.1$- $Na_v1.9$) (Figure S7A, blue arrow). Moreover, a hydrogen-bond between Tyr304 (α-subunit) and Glu48 (β1-subunit) that supports binding of the β1 subunit in $Na_v1.7$ is also missing in $Na_v1.5$, where the equivalent position is occupied by Leu316 (Figure S7A, red arrow). These structural changes suggest why $Na_v1.5$ cannot form the same regulatory interface with $Na_V\beta$ subunits as other Na_V α subunits.

Unlike β1, the $Na_V\beta2$ subunit forms a disulfide bond with the α-subunit of neuronal sodium channels (Isom et al., 1995; O'Malley and Isom, 2015). Surprisingly, we found that the disulfide bond-forming Cys895 from $Na_v1.7$ (Shen et al., 2019) is replaced by Leu869 in $Na_v1.5$ (Figure 1D, tan; Figure 1E, lower panel; Figure S7B, cyan arrow). This Cys residue is conserved in all other Na_V channels except $Na_v1.8$, which has Ala822 at the same position (Figure S7B, cyan arrow). This finding indicates that the β2 subunit does not form a disulfide linkage at this position with either the $Na_v1.5$ or $Na_v1.8$ α subunit. Together with the placement of a blocking glycosyl moiety in the binding site for the β1 subunit, these results establish a structural basis for reduced binding and modulation of $Na_V1.5$ by β subunits.

Structural Basis for Tetrodotoxin Selectivity at Its Receptor Site in the Outer Pore

The classic sodium channel blocker tetrodotoxin (TTX) binds in the outer mouth of the ion selectivity filter (SF) and blocks the pore (Hille, 1975b; Terlau et al., 1991). Its characteristic low affinity for $Na_V1.5$ channels (2 μM) compared to sodium channels in nerve and skeletal muscle (4–10 nM) is a hallmark of sodium channel pharmacology, determined primarily by substitution of a single amino acid residue ((Figure S7C); (Fozzard and Hanck, 1996; Sivilotti et al., 1997)). The overall structure of the SF of $rNa_v1.5_C$ is nearly identical to that of $Na_v1.7$, which has a high affinity for TTX (Figure 1F; Figure S7C). However, $rNa_v1.5_C$ shows clear density for Cys374 and Arg377 on the extracellular side of Asp373 (Figure 1G), in positions where $Na_v1.7$ has Tyr362 and Asn365 (Shen et al., 2019). Tyr362 helps TTX bind tightly to $Na_v1.7$ through a n-n stacking interaction, which is missing in $Na_V1.5$ (Figure 1G). The lack of this key interaction reduces the binding affinity of $rNa_v1.5_C$ for TTX by up to 500-fold (Sunami et al., 2000; Walker et al., 2012). Therefore, this residue is the structural

determinant that differentiates the TTX-insensitive sodium channels ($Na_v1.5$ and $Na_v1.8–9$) with a Cys or Ser from the TTX-sensitive channels ($Na_v1.1–1.4$, $Na_v1.6$ and $Na_v1.7$) with a Tyr or Phe. Our $rNa_v1.5_C$ structure shows that this amino acid substitution does not alter local protein conformation but eliminates a key side chain interaction with bound TTX by removing the aromatic side chain.

Structural Basis for Antiarrhythmic Drug Block of the Inner Pore

Class I antiarrhythmic drugs terminate and prevent cardiac arrhythmias by blocking cardiac sodium channels in a complex state-dependent manner (Sampson and Kass, 2011). They are divided into three classes (IA, IB, and IC) based on their rates of binding and unbinding, which determine their clinical uses (Sampson and Kass, 2011). The Class IC antiarrhythmic drug flecainide (Figure 2B) blocks cardiac sodium channels and is widely used to treat atrial arrhythmias, including the increasingly common problem of atrial fibrillation (Anno and Hondeghem, 1990; Konzen et al., 1990; Sampson and Kass, 2011). Flecainide blocks $rNa_V1.5_C$ with IC_{50}=16.6 μM when tested with depolarizing stimuli at 100 Hz (Figure S1B). The EC_{50} was increased to 140 μM when single stimuli were applied (Figure S1C), consistent with state- dependent block of open and inactivated $rNa_V1.5_C$, as observed for native $Na_V1.5$. Flecainide binds in the central cavity of $rNa_V1.5_C$, just on the intracellular side of the SF (Figure 2C, 2D). Its piperidine ring lies across the top of the central cavity, hindering exit of Na^+ from the SF (Figure 2C, 2D). The positively charged piperidine nitrogen points upward toward the inner exit from the SF, and the hydrophobic edge of the piperidine ring extends toward the phenyl sidechain of Phe1762 in the IVS6 segment (Figure 2C). This binding pose for flecainide is consistent with previous structure-function studies of $Na_V1.5$ (Liu et al., 2003a; Ragsdale et al., 1996; Wang et al., 2003) and with the less well-resolved binding pose of flecainide in Na_VAb (Gamal El-Din et al., 2018). Phe1762 may interact more strongly with the bound drug in the fully inactivated state observed in Na_VAb, in which two S6 segments move toward the pore axis (Payandeh et al., 2012).

The wall of the central cavity of Na_V channels is penetrated by four fenestrations that lead inward from the lipid bilayer between two PM (Pan et al., 2018; Payandeh et al., 2011; Shen et al., 2019). The two hydrophobic trifluoroethyoxy tails of flecainide latch onto the inner end of the fenestration between the PM in *DII* and *DIII* (Figure 2C, 2E). Flecainide can enter the central cavity through the fenestration and bind to its receptor site in Na_VAb (Gamal El-Din et al., 2018). Flecainide may access its binding site by entering through the fenestration between *D*II and *D*III in the PM of $Na_V1.5$ (Figure 2D, 2E). Entry is also possible through other fenestrations, including *D*III-*D*IV as suggested by molecular modeling studies based on $Na_V1.4$ (Nguyen et al., 2019), but the *D*II-*D*III fenestration is the largest and *D*III-*D*IV is significantly smaller in $rNa_V1.5_C$.

Arrhythmia Mutations in $Na_V1.5$

$Na_V1.5$ and the $Na_Vβ$ subunits are molecular targets for mutations that cause cardiac arrhythmias (Kapplinger et al., 2010; Li et al., 2018; Liu et al., 2003b; O'Malley and Isom, 2015). There are over 400 disease mutations of human $Na_v1.5$ (UniProt database), including 230 mutations in Brugada Syndrome Type-1 (BS1), 153 in Long QT Syndrome Type-3 (LQT3), nine in Progressive Familial Heart Block Type-1A (PFHA1A), five in Sick Sinus

Syndrome 1 (SSS1), and ten in Atrial Fibrillation Type-10 (ATFB10) (Liu et al., 2003b). Our high-resolution structure of $rNa_v1.5_C$ provides a structural template for these disease mutations (Figure 3). The mutations are distributed in every structural component, but they are especially common in conserved regions of the VS, SF, activation gate, and fast inactivation gate. The structural basis for pathogenic effects of these mutations is considered in the sections below.

State Dependent Conformations of the VS

The S4 segment in the VS contains 4 to 8 repeats of a positively charged amino acid residue flanked by two hydrophobic residues (Catterall et al., 2017; Numa and Noda, 1986). It is exposed to aqueous clefts on its extracellular and intracellular ends, and it is sealed to prevent transmembrane movement of water and ions at the narrow (~ 5 Å) hydrophobic constriction site (HCS; Figure 1B; Figure 4A–D, yellow). The steep voltage dependence of activation results from outward movement of the positive gating charges (Figure 4A–D, blue) in the S4 segment across membrane electric field through the HCS. This charge movement was first measured as a small capacitive gating current in the squid giant axon (Armstrong and Bezanilla, 1973). Chemical labeling, disulfide crosslinking, and gating pore current studies directly detected the outward movement of the S4 segments and their gating charges during activation (DeCaen et al., 2011; DeCaen et al., 2009; DeCaen et al., 2008; Gamal El-Din et al., 2014; Yang et al., 1996; Yang and Horn, 1995). Previous bacterial and mammalian sodium channel structures have captured activated states of the VS, which are most stable at 0 mV (Pan et al., 2018; Payandeh et al., 2011; Shen et al., 2019). However, recent determination of the structure of the Na_vAb, captured in the resting state, revealed the structural basis for gating charge movement, and supported the “sliding helix” model for VS activation, in which the gating charges move through the HCS under the influence of the electric field and exchange ion pair interactions with the intracellular negative cluster (INC) and extracellular negative cluster (ENC) of negatively charged amino acid residues (Figure 4A–D, red; (Wisedchaisri et al., 2019; Yarov-Yarovoy et al., 2012).

As expected from its negative voltage dependence of activation (Figure S1A), all four VS in $rNa_v1.5_C$ are in activated states (Figure 4A–D, left panels). The VS of *DI* closely resembles the activated state of Na_VAb (Figure S7D) (Payandeh et al., 2011) and other mammalian sodium channels (Pan et al., 2018; Shen et al., 2019). The *D*I gating charges R1-R3 point up toward the extracellular side above the HCS, and both R2 and R3 interact with the ENC. K4 is on the intracellular side of the HCS, stabilized by interaction with the INC (Figure 4A, left panel). Similar to *D*I, gating charges R1-R3 of the *D*II VS are also on the extracellular side of the HCS, but their outward translocation is less than in *D*I. R1 and R2 interact with the ENC, but R3 is just above the HCS, and K4 is still on the intracellular side of the HCS (Figure 4B, left panel). In contrast, the VS of *D*III is more activated. Four gating charges (K1-R4) are on the extracellular side of the HCS and both R3 and R4 have moved far enough outward to interact with the ENC. R5 is located in the HCS forming a n-cation interaction with Phe1252 (Figure 4C, left panel). Four gating charges in *D*IV (R1-R4) are on the extracellular side of the HCS, while R5 and R6 are on the intracellular side interacting with the INC (Figure 4D, left panel). In addition, two more conserved positively charged residues (Lys1643 and Arg1646) that continue the S4 helix on the intracellular side of the

HCS and could potentially serve as gating charges K7 and R8 (Figure S7E). In our structure, R8 serves as the C-cap, directed toward S4 helix dipole to stabilize the helical conformation (Figure S7E). These additional potential gating charges indicate that S4 of *D*IV VS could undergo larger outward movement during depolarization.

Recent structure determination of the resting state of Na_VAb (Wisedchaisri et al., 2019) allows us to view the conformational change associated with activation of the four VS of $Na_V1.5$. We generated a resting state model for each VS of $Na_v1.5_C$ by aligning the amino acid sequence of each individual VS with the VS of Na_VAb and using MODELLER to determine the best fit structure of the VS of $Na_v1.5_C$ (Figure 4A–D, right panels). We found that two gating charges from each VS of $Na_v1.5_C$ moved inward through the HCS, consistent with the Na_VAb resting state structure. These results suggest that the gating charge movements observed in the transition to the resting state in Na_VAb also apply to $Na_V1.5$.

In contrast to bacterial sodium channels, whose VS are identical and activate stochastically, the four VS in eukaryotic sodium channels are nonequivalent and activate sequentially (Chanda and Bezanilla, 2002). Our $rNa_v1.5_C$ structure reveals the asymmetric conformation of the four VS that leads to sequential voltage-dependent activation. Fluorescent labeling and gating pore current studies showed that the S4 segment in the VS of *D*IV moves five-fold slower than the other three S4 segments (Capes et al., 2013; Chanda and Bezanilla, 2002; Goldschen-Ohm et al., 2013). During depolarization, the VS of *D*I, *D*II and *D*III move S4 quickly outward to activate the channel, and subsequently full activation of the *D*IV VS induces a conformational change that leads to fast inactivation. *D*I VS and *D*II VS also recover quickly from inactivation, whereas *D*III VS and *D*IV VS recover more slowly. Because *D*III VS and *D*IV VS have more gating charges than *D*I VS and *D*II VS, translocating these additional gating charges across the HCS may be the rate limiting step for their S4 movement.

Arrhythmia Mutations in the VS

To understand better how mutations in the VS cause arrhythmias, we compared the positions of the affected amino acid residues in our activated state structure of $Na_V1.5_C$ with their positions in the modeled resting state of the VS of $Na_V1.5_C$. We found that 18 of 24 mutations in the S3 and S4 segments that we examined moved greater than 4 Å between the resting and activated state conformations (Table 1). Mutations of these amino acid residues that move substantially during activation and deactivation of the voltage sensor likely cause dysfunction by altering the normal conformational changes that are required for VS function. Moreover, the six residues with arrhythmia mutations that moved smaller distances might perturb movement of the VS by altered interactions of their mutant sidechains with neighboring amino acid residues that do undergo substantial movements during VS function.

Mutations of Arg gating charges in $Na_V1.4$ cause pathogenic gating pore current in Hypokalemic and Normokalemic Periodic Paralysis owing to leak of ions through the mutant VS (Sokolov et al., 2007, 2008; Struyk and Cannon, 2007). The hole in the center of the VS that conducts pathogenic gating pore current in the mutants was visualized by X-ray crystallography of Na_VAb, revealing an aqueous conducting pathway 2–3 Å in diameter

(Jiang et al., 2018). Nine VS mutations in $Na_V1.5$ convert a gating charge Arg to another uncharged residue and therefore are candidates to conduct gating pore current (Moreau and Chahine, 2018). Two of these mutant channels have been shown to conduct substantial gating pore current by direct electrophysiological measurements (Moreau et al., 2015). We introduced the mutation R225P at the position of R3 in our $rNa_V1.5_C$ structure (R226P in rat) and examined the resulting model with MOLE2 to detect water-filled space. As for HypoPP mutations, we found that the pathogenic arrhythmia mutation R226P does indeed make a conductive hole 2.2 Å in diameter through the VS in Oil of $rNa_V1.5_C$ (Figure 4G, H). As expected from electrophysiological studies, this conduction pathway through the mutant VS is open in the activated state but not in the resting state (Figure 4G, H). These results define the structural basis for pathogenic gating pore current in cardiac arrhythmias.

Intracellular Activation Gate

The intracellular activation gate formed by the intracellular ends of the S6 transmembrane segments controls sodium channel opening and closing, which are coupled to voltage-dependent conformational changes in the VS through the S4-S5 linker, as we observed by comparing the resting and open states of Na_VAb (Wisedchaisri et al., 2019). Our $rNa_v1.5_C$ structure has a partially open pore, with a water-accessible diameter inside the activation gate of 5.6 Å calculated by MOLE2 (Figure 5A–B). When compared with the open-state structure of Na_vAb, which has a water-accessible diameter of 8.0 Å, the 5.6 Å opening of the activation gate of $rNa_v1.5_C$ would not be wide enough to allow uninterrupted diffusion of hydrated Na^+. Movements of the S4-S5 linkers of *D*II, *D*III, and *D*IV toward the center of the activation gate also indicate that the gate is not fully open (Figure 5B).

In order to investigate the closed pore structure of the $rNa_v1.5_C$, a resting state pore model was generated by MODELLER based on the resting state structure of Na_vAb. Ths the activation gate. As a consequence, the gate is completely sealed by the sidechains of a ring of hydrophobic residues (Val413, Leu941, Ile1471 and Ile1773) (Figure 5C). This closed and sealed model of the resting state has no aqueous space for water or ions to penetrate the closed activation gate.

Fast Inactivation and Its Coupling to Voltage Sensing and Activation

Cardiac sodium channels are inactivated within 1–2 ms after opening. Fast inactivation of sodium channels decreases Na^+ influx and allows potassium channels to activate and repolarize the membrane potential. This mechanism is very important for generating repeated action potentials to drive the heartbeat at a consistent frequency. Mutagenesis studies indicated that an isoleucine-phenylalanine-methionine (IFM) motif located in the *D*III-*D*IV linker is responsible for fast inactivation of eukaryotic sodium channels (West et al., 1992), through interactions with amino acid residues in the S4-S5 linkers in *D*III and *D*IV and the intracellular ends of the S5 and S6 segments of *D*IV (Kellenberger et al., 1996; McPhee et al., 1998; McPhee et al., 1994, 1995; Smith and Goldin, 1997). Site-directed fluorescent labeling and gating-pore current studies suggested that fast inactivation is coupled with the movement of *D*III and *D*IV gating charges and causes immobilization of those gating charges (Capes et al., 2013; Chanda and Bezanilla, 2002).

In our rNa$_v$1.5$_C$ structure, the *D*III-*D*IV linker, which is responsible for fast inactivation, packs in parallel with *D*IV S4-S5 linker, and the IFM motif dips into a pocket formed by *D*III S6 and *D*IV S5 and S6 (Figure 5A). The IFM motif is well resolved with unambiguous electron density (Figure 5D). Remarkably, its structure closely resembles the structure of the IFM motif determined by NMR analysis in solution (Rohl et al., 1999), indicating that its fold is highly stable. IFM penetrates into a compact hydrophobic pocket ~8 Å deep formed by the S4-S5 linker from *D*IV, S5 from *D*III, and S5 and S6 from *D*IV (Figure 5E), in close agreement with mutagenesis studies (Kellenberger et al., 1996; McPhee et al., 1998; McPhee et al., 1994, 1995; Smith and Goldin, 1997). Besides the hydrophobic interaction inside this pocket, additional interactions from both ends stabilize binding of the IFM motif. At its C-terminus, Asn1661, the carbonyl oxygens of Phe1488 and Thr1490, and the carbonyl oxygen of Gln1320 form two hydrogen bonds (Figure 5F and G). Interactions with a cluster of hydrophobic residues further stabilizes binding of the *D*III-*D*IV linker to the *D*IV S4-S5 linker (Figure 5F). At its N-terminus, Asn1474 and Gln1478 from *D*III S6 interact with carbonyl oxygens of Gly1338 and Ala1328, respectively (Figure 5G). Mutations of those interacting residues disrupt binding of the IFM motif, which in turn affect sodium channel inactivation. For instance, the single mutation Asn1661Ala or the double mutations Phe1650Ala and Leu1659Ala almost completely abolish fast inactivation (McPhee et al., 1998; McPhee et al., 1994, 1995; Smith and Goldin, 1997).

The sequential activation of the four VS in mammalian sodium channels finishes with activation of *D*IV VS, which is thought to be the main driving force for fast inactivation (Capes et al., 2013; Goldschen-Ohm et al., 2013). *D*III VS, which is activated third in sequence, is also involved in fast inactivation, and its gating charges are stabilized in their outward positions by fast inactivation. By comparing the VS of rNa$_v$1.5$_C$ *D*III with the activated VS of Na$_v$Ab, we found that the gating charges of rNa$_v$1.5$_C$ *D*III VS have moved further outward than those of Na$_v$Ab, thereby lifting S4-S5 linker of *D*III more outward with respect to the intracellular membrane surface (Figure 4E) and opening a tight binding pocket for the IFM motif. Thus, *D*III VS must be activated to move its S4-S5 linker into the proper position for binding the IFM motif. The binding energy of the IFM motif would stabilize this activated state of the *D*III VS, revealing why movement of the gating charges of DIII VS is slower than *D*I and *D*II during recovery from inactivation (Capes et al., 2013; Goldschen-Ohm et al., 2013).

Our rNa$_v$1.5$_C$ structure shows the IFM motif binding to the pocket on the periphery of the activation gate, which is consistent with the structures of human Na$_v$1.2, Na$_v$1.4 and Na$_v$1.7 (Pan et al., 2019; Pan et al., 2018; Shen et al., 2019). Those similar structures demonstrate a conserved mechanism for fast inactivation. Moreover, the close interactions of the IFM motif detailed here for rNa$_v$1.5$_C$ (Figure 5D–G) suggest that the inactivation gate is in an inactivating conformation because it interacts directly with several amino acid residues in the “inactivation gate receptor” whose mutation disrupts fast inactivation (McPhee et al., 1998; McPhee et al., 1994, 1995; Smith and Goldin, 1997). Inactivation is evidently triggered by outward movement of the gating charges of *D*III and *D*IV VS, which move the IFM motif into the binding pocket (Kellenberger et al., 1996) and decouple the *D*III S4-S5 linker from *D*IV S6. In rNa$_v$1.5$_C$, we observe that the *D*III S4-S5 linker shifts significantly toward the center of the activation gate, compared with the other three S4-S5 linkers (Figure

5A, B). In this position, the activation gate cannot open wide enough for free conductance of hydrated Na^+ (Chakrabarti et al., 2013). Thus, our structure suggests that $Na_V1.5_C$ is in an intermediate inactivated state because the fast inactivation gate is not as far open as observed in the Na_VPas channel from cockroach (Shen et al., 2017), and the pore is not yet as completely closed as in the inactivated state of Na_VAb (Payandeh et al., 2012).

Arrhythmia Mutations in the Fast Inactivation Gate and Its Receptor

LQT3 and other cardiac arrhythmias are often caused by mutations that slow or prevent fast inactivation (Li et al., 2018). LQT3 mutants are most often located in the inactivation gate or its receptor (Figure 3). Given their short lengths, it is surprising that 11 arrhythmia mutations are located in the S4-S5 linkers in *D*I, *D*III, and *D*IV (Figure 3). Nine of these mutations cause LQT3 by impairing fast inactivation. Our structure of $Na_V1.5$ gives clear insight into the mechanism of action of these mutations (Figure 5E–G). These amino acid substitutions would impair the close fit of the IFM motif into its receptor site by altering the collar of S4-S5 segments that form the receptor. The LQT3 mutant Ile1662Val (Ile1660Val in $hNa_v1.5$) may cause reduced amplitude of sodium current because the IFM motif binds deeper and makes recovery from fast inactivation more difficult.

Mutations in the inactivation gate itself also cause LQT3. For example, Phe1475Cys (Phe1473Cys in $hNa_v1.5$) alters the key Phe in the IFM motif (Figure 5D and E) and causes slowed and incomplete inactivation and increased persistent sodium current (Bankston et al., 2007). The nearby ATFB10 mutant Gln1478Lys (Gln1476Lys in $hNa_v1.5$; Figure 5G) also accelerates recovery from fast inactivation, due to decreased affinity for IFM (Dichgans et al., 2005). The original LQT3 triple mutation, ΔKPQ(1507–1509), causes a three-residue in-frame deletion downstream from the inactivation gate and dramatically impairs fast inactivation (Bennett et al., 1995). This deletion mutation of $rNa_v1.5_C$ is located in the flexible loop following the highly conserved a-helix in the *DIII-DIV* linker (Figures 1B and 3C), which would shorten the loop by 13 Å and significantly limit the movement of IFM during cycles of activation followed by fast inactivation in the repeated cardiac action potentials necessary to trigger the heartbeat.

Structure of the Ion Selectivity Filter

The location of the SF was first revealed by mapping the binding site for TTX (Noda et al., 1989; Terlau et al., 1991). Mutagenesis studies identified amino acid residues from equivalent positions in the four domains, Asp373-Glu901-Lys1421-Ala1713 (DEKA), as the key determinants of Na^+ selectivity (Favre et al., 1996; Heinemann et al., 1992; Sun et al., 1997). In NaVAb, this highly charged site at the extracellular entry to the SF, termed the high field strength site (HFS), is formed by four Glu177 sidechains. This site interacts first with permeating Na^+ and catalyzes partial dehydration of the conducted ion (Chakrabarti et al., 2013). In the $rNa_v1.5_C$ structure, the DEKA motif stands in the center of the pore, forming a similar HFS (Figure 6A, B). The conformations of the four Ca atoms form a nearly four-fold symmetrical square, similar to the conformation of the HFS in Na_VAb (Payandeh et al., 2011), but the difference in sidechains makes the site in $rNa_v1.5_C$ asymmetric. The high local resolution for the SF structure allows us to build a reliable atomic model of these sidechains (Figure 6B). Unambiguous density for Lys1421 shows the

sidechain pointing inward, deep into the SF as a pinch point (Figure 6B–D). This position for the sidechain of Lys1421 is surprising, as it seems likely that cation permeation would be blocked if a full positive charge were located in this position. The electron density for the distal end of the sidechain of Glu901 is not as well resolved, which suggests sidechain flexibility. This conformational flexibility of Glu901 may allow it to function via the "sidechain-dunking" mechanism of Na^+ permeation observed in molecular dynamics studies of Na_VAb, in which rotation of the corresponding Glu177 side chains at a single torsion angle allowed their negative charges to "dunk" in concert with movement of Na^+ through the SF (Chakrabarti et al., 2013).

Compared to the approximately square orifice of the SF of Na_VAb (Payandeh et al., 2011), which has van der Walls dimensions of 4.6 × 4.6 Å, $rNa_v1.5_C$ has a rectangular SF with van der Walls dimensions of 3.0 × 4.6 Å (Figure 6B–C). These dimensions are remarkably close to the model developed from classic studies of selective permeation of inorganic and organic cations, which suggested 3.1 × 5.1 Å (Hille, 1971, 1972, 1975a). In contrast to the four Glu177 residues that form the HFS in Na_VAb, the Asp373 and Glu901 sidechain positions are more inward in $Na_V1.5$, and the other half of the negatively charged tetrad is replaced by Lys1421 and Ala1713 on the opposite side of the SF. However, the HFS of $Na_v1.5$ is extended inward by the sidechains of Glu376, Asp904 and Asp1716 (Figure 6D), which may act together with Asp373 and Glu901 to form the asymmetric HFS of $Na_V1.5$.

Arrhythmia Mutations in the Pore and Selectivity Filter

A remarkable panel of 71 arrhythmia mutations target the PM and SF (Figure 3). Most of these mutations cause Brugada Syndrome (Figure 3, red), which is thought to arise from heterozygous loss of function of $Na_V1.5$ by impairing its folding and functional expression (Baroudi et al., 2002; Baroudi et al., 2001). However, mutations in key amino acid residues in the PM may also cause loss of function by impairing ion conductance through an otherwise structurally normal $Na_V1.5$ channel protein. We found eight Brugada Syndrome mutations in the SF itself, and our structure gives clear insights into the likely pathogenic mechanism for five of them.

Two Brugada Syndrome mutations are likely to have local structural effects that impair ion conductance. The mutation Trp375Gly removes the large indole sidechain from this highly conserved Trp residue, whose backbone carbonyl is crucial in stabilizing the SF structure by forming a network of hydrogen bonds around the HFS (Payandeh et al., 2011). It is likely that this mutation alters the square shape of the four Cα atoms that form the backbone corners of the SF. The nearby mutation Met370Lys replaces a hydrophobic sidechain with a hydrophilic one in a buried hydrophobic pocket. This mutation may also alter the precise local folding of the SF.

Even more strikingly, we found that the key SF DEKA signature residue Lys1421 in *D*III is actually a target for Brugada Syndrome mutation (Lys1421Glu; (Kapplinger et al., 2010)). As our structure reveals, this residue plays a key role in forming the HFS in the SF of $Na_V1.5$, and functional studies show that it is essential for selective sodium conductance (Favre et al., 1996; Heinemann et al., 1992). It occupies a unique dunked position deep in the SF in our structure, and we propose that it has a unique function as a coordinating ligand

for Na^+ through delocalization of its positive charge by formation of a charge transfer complex, as developed in more detail in the following section. Our structure predicts that mutation of Lys1421 to Glu, as in Brugada Syndrome, would create an ion coordination site for Ca^{2+} in the SF and thereby cause a loss of function by competing with sodium conductance, as was shown in mutagenesis studies of $Na_V1.4$ (Heinemann et al., 1992). Thus, our structure defines the molecular basis for $Na_V1.5$ dysfunction caused by this Brugada Syndrome mutation at the atomic level. The adjacent Gly is the target of the Brugada Syndrome mutation Gly1422Arg. This mutation in *D*III places the large positively charged Arg sidechain squarely in the aqueous ion conduction pathway and would surely reduce or prevent sodium conductance. Finally, the Brugada Syndrome mutation Thr1711Arg in *D*IV has a similar effect to Gly1422Arg in *D*III by placing a positively charged Arg sidechain in the aqueous ion conduction pathway in the SF, thereby reducing or blocking sodium conductance.

Sidechain Dunking and Interaction with Lys1421 During Sodium Permeation

It is surprising that bacterial channels have a HFS formed by four negatively charged Glu sidechains, whereas vertebrate sodium channels have a signature sequence of DEKA at the HFS. Is there a common mechanism that mediates conduction in both cases? Our previous crystal structure of Na_vAb and correlated molecular dynamics simulations suggested that hydrated Na^+ is partially dehydrated by the HFS formed by four Glu177 residues and further that Glu177 sidechains rotate around a single torsion angle and “dunk” with permeating Na^+ (Chakrabarti et al., 2013). The most common modes of Na^+ conductance have two dunking Glu177 carboxyl groups (Chakrabarti et al., 2013). In the structure of the SF in $Na_V1.5_C$, Lys1421 is in a dunked conformation, as if it interacts with permeating Na^+. How is that possible? Detailed analysis of the pKa’s of Lys residues in different positions in a known protein structure demonstrated large decreases in pKa of the Lys $-NH_2$ group to values as low at pH 5.3 in nonaqueous environments and in environments with nearby hydrogen bond acceptors, comparable to the pKa values of carboxyl groups (Isom et al., 2011; Wu et al., 2017). In the SF itself, there are no free water molecules and many surrounding hydrogen bond acceptors (Figure 6B–E). Therefore, we propose that Lys1421 sidechain dunked deep in the SF forms a complex in which its positive charge is delocalized by interaction of all three NH_3^+ protons with nearby backbone carbonyl groups of Thr1419, Thr1711, and Ser1712 (Figure 6E). Remarkably, despite the presence of Lys1421, the surface of the SF in this region is uniformly electronegative (Figure S7F, red). This delocalization of the $-NH_3^+$ charge may allow the unpaired electrons of the N atom to serve as a specific coordinating ligand of Na^+, consistent with the unique requirement for Lys at this position for Na^+ selectivity (Favre et al., 1996; Heinemann et al., 1992; Sun et al., 1997). Based on these considerations, we propose a unified model for SF function in prokaryotes and eukaryotes in which Na^+ is conducted in concert with dunking of the sidechain of Glu901 followed by formation of a unique charge-delocalization complex with Lys1421 in eukaryotes. This model retains the sidechain dunking mechanism of prokaryotic sodium channels and explains the extraordinary importance for Lys1421 in determining the Na^+ selectivity of eukaryotic sodium channels, because only charged Na^+ would have small enough size and sufficiently high field strength to join the charge delocalization complex formed by Lys1421 and engage in an energetically favorable coordination with it. Consistent with this model, Li

$^{+}$ is also highly permeant and has a similar high field strength surrounding its positively charged nucleus, whereas the larger alkali metal cations K^+, Rb^+, and Cs^+ are not highly permeant and do not have a high-field-strength positive charge. Thus, this model for sodium selectivity would bring together several unexpected aspects of sodium permeation, the sidechain-dunking mechanism of the prokaryotic SF, and the unique structure of the eukaryotic SF.

CONCLUSIONS

The $Na_V1.5$ channel has unique physiological roles and stands alone on a branch of the dendrogram of related sodium channel proteins (Goldin et al., 2000). Even heterozygous disease mutations in $Na_V1.5$ can be lethal, indicating that other sodium channels cannot compensate for loss of its unique functions. Despite these specific functional requirements, our structure of $Na_V1.5_C$ is highly similar to other sodium channels in the transmembrane core. Based on this detailed structure, we have elucidated the molecular basis for several specific functions of $Na_V1.5$.

The interaction sites for $Na_V\beta$ subunits are strikingly altered in $Na_V1.5_C$. An Asn residue with N-linked carbohydrate chain attached is substituted for a key amino acid residue in the interaction site for the β1 subunit. Differential glycosylation of this site has the potential for controlling modulation of sodium channel expression and function by β1 and β3 subunits. Similarly, the highly conserved Cys that forms a disulfide bond with the β2 and β4 subunits is replaced by Leu869. The lack of disulfide-bond formation is likely to make binding of β2 and β4 much less stable.

The characteristic low affinity for block of $Na_V1.5$ by TTX is a hallmark of sodium channel pharmacology. The $Na_V1.5_C$ structure shows that the Cys374 residue that is substituted for aromatic residues in $Na_V1.5$ does not change the local conformation but fails to make a productive molecular interaction with bound TTX because of steric constraints. The loss of interactions between TTX and the aromatic side chains at this position is likely to be responsible for the 500-fold reduction of TTX-binding affinity in $Na_V1.5$.

Our results give a detailed, high-resolution view of the receptor site for antiarrhythmic drugs. Flecainide binds to a platform at one side of the central cavity and blocks sodium permeation directly. Binding of its piperidine nitrogen to the Lys1421 charge delocalization complex at the inner end of the SF would prevent conductance of Na^+. This platform may mediate binding of other Class IC antiarrhythmic drugs, most of which have a large hydrophobic ring structure similar to flecainide. The Class IA antiarrhythmic drugs (eg., procainamide) and the Class IB antiarrhythmic drugs (eg. lidocaine) are smaller and less hydrophobic; therefore, it is likely that they occupy only a portion of the flecainide-binding surface. The comparatively high affinity and slow binding kinetics that are the hallmark of block by flecainide and other Class IC drugs likely reflect their interaction with this larger binding surface.

The four VS in the $rNa_V1.5_C$ are all in partially or fully activated conformations, because each of them has moved at least two gating charges outward with respect to their positions in

our resting state model of $Na_V1.5$. The outward position of the gating charges is most prominent for the VS in *D*III because four gating charges are located outside the HCS. This outward movement of the S4 segment in *D*III is coupled to conformational changes in the S4-S5 linkers that form the receptor site for the IFM motif in the fast inactivation gate. In the resting state model of $Na_V1.5$, the interaction site for the inactivation gate is blocked by the intracellular end of the S4 segment in *D*III and the S4-S5 linker connecting *D*III and *D*IV, but it is available and occupied by the IFM motif of the inactivation gate in our structure of $Na_V1.5_C$. These structural results reveal the molecular basis for coupling of activation to fast inactivation in atomic detail.

The structure of the SF in $rNa_V1.5_C$ reveals crucial insights into the mechanism of Na^+ conductance and selectivity. The image of the sidechain of Lys1421 in a dunked conformation deep in the SF leads directly to a model of cation permeation that combines two key elements: dunking of the sidechain of Glu901, in analogy to the model proposed for bacterial sodium channels from molecular dynamics analysis (Chakrabarti et al., 2013), plus interaction with the unique charge-delocalization complex of the amino group of Lys1421 and its neighboring hydrogen bond acceptors. As illustrated in Figure S7F, the positive charge of Lys1421 is completely transferred to the three backbone carbonyls with which it forms hydrogen bonds, leaving a negative surface for interaction with conducted cations. Among alkali metal cations, only Li^+ and Na^+ have sufficient charge density to replace a proton as a ligand of a primary NH_2 group. Thus, this model explains the unique requirement for Lys1421 in order to achieve high Na^+ selectivity and fits well with the high conductance of Li^+ in sodium channels.

Finally, the structure of $rNa_V1.5_C$ provides key insights into the mechanism of action of arrhythmia mutations. We find that many mutations located in the VS affect amino acid residues that move substantially during activation. Changing these amino acid residues is likely to disrupt activation and/or deactivation by altering structural interactions that are essential for normal VS movement. Arrhythmia mutations that cause gating pore currents generate a transmembrane hole in the VS, like corresponding mutations in $Na_V1.4$ that are pathogenic in periodic paralysis (Jiang et al., 2018). This finding elucidates the mechanism of arrhythmogenesis by these mutations at the atomic level. We find that mutations that alter amino acid residues in the fast inactivation gate and its receptor disrupt close interactions between the IFM motif and its binding partners in the S4-S5 linkers in *D*III and *D*IV and the intracellular end of the S6 segment in *D*I. Similarly, mutation of the key SF residue Lys1421 to Glu may cause loss of function by inducing a calcium binding site in a blocking position in the SF. Future experiments may allow structure-based diagnosis and drug development for life-threatening cardiac arrhythmias based on this structural information.

STAR METHODS

LEAD CONTACT AND MATERIALS AVAILABILITY

Further information and requests for resources and reagents should be directed to and will be fulfilled by the Lead Contact, William A. Catterall (wcatt@uw.edu). All unique/stable reagents generated in this study are available from the Lead Contact with a completed Materials Transfer Agreement.

EXPERIMENTAL MODEL AND SUBJECT DETAILS

Microbe strains—*E. coli* GC10 was cultured at 37°C in LB medium supplemented with 100 μg/mL of ampicillin for plasmid DNA extraction. *E. coli* DH10Bac was cultured at 37°C in LB medium supplemented with 50 μg/mL kanamycin sulfate, 7 μg/mL gentamicin and 10 μg/mL tetracycline for bacmid production.

Cell lines—Sf9 *(Spodoptera frugiperda)* insect cells were maintained in Grace's Insect Medium and supplemented with 10% FBS and penicillin/streptomycin at 27°C and passaged at 80–95% confluence for baculovirus production. HEK293S GnTI$^-$ *(Homo sapiens)* mammalian cells were maintained and infected on cell culture plates in Dulbecco's Modified Eagle Medium (DMEM) supplemented with 10% FBS and glutamine/penicillin/streptomycin at 37°C and 5% CO_2 for electrophysiology.

METHOD DETAILS

Electrophysiological Recordings—All experiments were performed at room temperature (21–24°C). HEK293S GnTI$^-$ cells were held at −140 mV and 50-ms pulses were applied in 10 mV increments. Holding leak potential was set to −140 mV. Extracellular solution contains in mM: 140 NaCl, 2 $CaCl_2$, 2 $MgCl_2$, 10 HEPES, pH 7.4. Intracellular solution: 35 NaCl, 105 CsF, 10 EGTA, 10 HEPES, pH 7.4. Glass electrodes had a resistance 2–3 MW. Currents resulted from applied pulses were filtered at 5 kHz with a low-pass Bessel filter, and then digitized at 20 kHz. Voltage commands were generated using Pulse 8.5 software (HEKA, Germany) and ITC18 analog-to-digital interface (Instrutech, Port Washington, NY).

Rat $Na_v1.5$ Expression and Purification—The full-length rat Nav1.5 gene was cloned into pEG_BacMam vector, with a recombinant human rhinovirus (RHV 3C) protease site, eGFP and a DYKDDDK FLAG peptide fused at its C-terminus. Non-structured loop deleted constructs were screened by fluorescence-detection size- exclusion chromatography (FSEC) (Kawate and Gouaux, 2006) for improved expression level and thermostability. The plasmid was transfected into DH10Bac competent cells to make baculovirus for transduction of HEK293S GnTI$^-$ cells (ATCC). HEK293S GnTI− cells were cultured in FreeStyle 293 expression medium (ThermoFisher Scientific) within 8% CO_2 37 °C incubator shaking at 130 rpm. 30 mL of β3 baculovirus was added to 800 mL medium when cell density reached 2.5–3.0 × 10^6 cells per mL. 10 mM sodium butyrate was added to cell culture 8 hours after and cells were cultured for another 48 h at 30 with 8% CO_2 before harvesting.

For each purification, 6 L 0of transfected cells were harvested and washed with buffer containing 25 mM HEPES pH = 7.4, 150 mM NaCl and 10% glycerol (buffer A). Washed cells were collected by ultra-centrifugation at 100,000xg for 1 h, the cell pellet was resuspended in buffer A supplemented with 1% (w/v) n-dodecyl-p-D-maltopyranoside (DDM, Anatrace), 0.2% (w/v) cholesteryl hemisuccinate Tris salt (CHS, Anatrace), 5 mM lidocaine, and protease inhibitor cocktail (Sigma), and agitated for 1.5 h at 4°C. The supernatant was separated by ultra-centrifugation at 100,000×g for 35 min, then incubated with anti-Flag M2 affinity gel (Sigma) and agitated for 1 h at 4°C. The resin was re-loaded to a column and washed 5 times with buffer A supplemented with 0.06% glycol-diosgenin

(GDN, Anatrace) and 2 mM lidocaine in a total volume of 100 ml. The $rNa_V1.5_C$ protein was eluted with buffer A supplemented with 0.06% GDN, 2 mM lidocaine and 100 μg/mL Flag peptide (Bio Basic). The eluted protein was concentrated and loaded onto a Superose-6 column (GE Healthcare) equilibrated with buffer containing 25 mM imidazole pH=6.0, 150 mM NaCI, 1 mM lidocaine and 0.006% GDN. Peak fractions were collected and concentrated to ~ 500 μgl at 1 mg/ml and mixed with 50 μgM ProTx II overnight. The mixture was then re-loaded to Superose-6 column within the same buffer. Finally, peak fractions were concentrated to 50 μgl at 4.5 mg/ml.

For $rNa_V1.5_C$-flecainide complex purification, the sample was purified similarly with some modifications. First, no lidocaine was used throughout the purification. Second, the sample was mixed with purified human FGF12b and incubated overnight at 4 °C. Third, the solutions for the second gel filtration contained 0.5 mM flecainide. Peak fractions were collected and concentrated to 50 μgl at 5.5 mg/ml.

CryoEM Grid Preparation and Data Collection—Three microliters of purified sample was applied to glow-discharged holey gold grids (UltraAuFoil, 300 mesh, R1.2/1.3), and blotted for 3.0 – 3.5 s at 100% humidity and 4°C before being plunge-frozen in liquid ethane cooled by liquid nitrogen using an FEI Mark IV Vitrobot. All data were acquired using a Titan Krios transmission electron microscope operated at 300 kV, a Gatan K2 Summit direct detector and Gatan Quantum GIF energy filter with a slit width of 20 eV. A total of 7,626 movie stacks for $rNa_V1.5_C$-ProTxII and 5,049 movie stacks for $rNa_V1.5_C$-flecainide were automatically collected using Leginon (Suloway et al., 2005) at a nominal magnification of 130,000x with a pixel size of 0.528 Å (super-resolution mode). Defocus range was set between −1.0 and −2.5 μm. The dose rate was adjusted to 8 counts/pixel/s, and each stack was exposed for 8.4 s with 42 frames with a total dose of 60 $e^-/Å^2$.

Cryo-EM Data Processing—The movie stacks were motion corrected with MotionCorr2 (Zheng et al., 2017), binned 2- fold, and dose weighted, yielding a pixel size of 1.056 Å. Defocus value of each aligned sum were estimated with Gctf (Zhang, 2016). For $rNa_V1.5_C$-ProTxII and $rNa_V1.5_C$-FGF12b-flecainide respectively, 7,427/4,890 micrographs with CTF fits better than 6 Å were used for particle picking. A total of 2,188,972/2,369,854 particles were automatically picked in RELION2.0 (Scheres, 2012). After several rounds of 2D classification, 590,667/1,164,667 good particles were selected and subjected to one class global angular search 3D classification with an angular search step at 7.5°, using the low-pass filtered cryoEM map of Na_VPas as an initial model. Each of the last five iterations was further subjected to four-class local angular search and 3D classification with an angular search step at 3.75°. After combining particles from the best 3D classes and removing duplicated particles, 293,629/733,541 particles were subjected to per-particle CTF estimation by Gctf followed by Bayesian polishing. The polished particles were subjected to a final three-class multi-reference 3D classification. The best class containing 106,104/513,604 particles was imported into cisTEM (Grant et al., 2018) for refinement. A protein-only mask was used to avoid over-fitting of the detergent micelles. Several iterative global and local refinement improved protein density of the map. For the $rNa_V1.5_C$-ProTxII map, only weak density for ProTxII was observed on DI-VS, which was not sufficient to

build a model. For the rNa$_V$1.5$_C$-FGF12b-flecainide map, weak density at the C-terminus was observed, but it was not sufficient to build a model for the CTD or FGF12b. The final map was sharpened in cisTEM by applying a B-factor of −60. Local resolution was estimated by MonoRes (Vilas et al., 2018). A diagram of data processing is presented in Figure S2 and Figure S5.

Model Building and Refinement—The structure of human Na$_V$1.4 (PDB code: 6AGF) α-subunit was fitted into the cryo-EM density map of rNa$_V$1.5$_C$ in Chimera (Pettersen et al., 2004). Then the model was manually rebuilt in COOT (Emsley et al., 2010) and subsequently refined in Phenix (Adams et al., 2010). The model vs map FSC curve was calculated by Phenix.mtriage. Statistics for cryo-EM data collection and model refinement are summarized in Supplementary Table S1.

QUANTIFICATION AND STATISTICAL ANALYSIS

Analysis of electrophysiological data—Current–voltage (I–V) relationships were recorded in response to voltage steps ranging from − 150 to + 50 mV in 10-mV increments from a holding potential of− 150 mV. Conductance-voltage (G-V) curves were calculated from the corresponding (I–V) curves. Pulses were generated and currents were recorded using Pulse software controlling an InstruTECH ITC18 interface (HEKA). Data were analyzed using Igor Pro 6.37 (WaveMetrics). G-V curves were fit with a simple two-state Boltzmann Equation $1/(1+\exp(V_{1/2}-V_p)/k)$ in which V_p is the stimulus potential, $V_{1/2}$ is the half-activation voltage, and k is the slope factor. Dose-Response curve was fit with a Hill equation $(\text{base}+(\text{max}-\text{base})/(1+K_A/[L])^n)$, where K_A is flecainide concentration producing 50% block and [L] is the free unbound flecainide, and n is the Hill coefficient. The best fit gives a Hill coefficient n= 0.75.

Estimation—Protein concentrations were calculated by an A280 extinction coefficient of 258,015 M^{-1} cm^{-1} from a spectrophotometer. Global resolution estimation of the cryo-EM density maps were based on the Fourier Shell Correlation criterion.

DATA AND CODE AVAILABILITY

The cryo-EM map of the rNa$_v$1.5$_C$ and rNa$_v$1.5$_C$/flecainide complex have been deposited in the Electron Microscopy Data Bank (EMDB) under accession code EMD-20951 and EMD-20949, respectively. The coordinates of the rNa$_v$1.5$_C$ and rNa$_v$1.5$_C$/flecainide complex atomic model have been deposited in the Protein Data Bank (PDB) under accession code 6UZ3 and 6UZ0, respectively.

Supplementary Material

Refer to Web version on PubMed Central for supplementary material.

Acknowledgements

We are grateful to Dr. Eric Gouaux (Vollum Institute, Oregon Health & Science University) and the staff at the Cryo-EM Facility of Oregon Health & Science University for their advice and help in the early phase of this work. We thank J. P. Quispe of the University of Washington Cryo-EM Facility for advice and technical assistance during the main phase of data collection and Dr. Jin Li, Department of Pharmacology, University of Washington, for

technical and editorial support. This research was supported by National Institutes of Health Research Grant R01 HL112808 (to W.A.C. and N.Z.) and by the Howard Hughes Medical Institute (N.Z.).

REFERENCES

Adams PD, Afonine PV, Bunkoczi G, Chen VB, Davis IW, Echols N, Headd JJ, Hung LW, Kapral GJ, Grosse-Kunstleve RW, et al. (2010). PHENIX: a comprehensive Python-based system for macromolecular structure solution. Acta Crystallogr D Biol Crystallogr 66, 213–221. [PubMed: 20124702]

Anno T, and Hondeghem LM (1990). Interactions of flecainide with guinea pig cardiac sodium channels. Importance of activation unblocking to the voltage dependence of recovery. Circ Res 66, 789–803. [PubMed: 2155069]

Armstrong CM, and Bezanilla F (1973). Currents related to movement of the gating particles of the sodium channels. Nature 242, 459–461. [PubMed: 4700900]

Bankston JR, Yue M, Chung W, Spyres M, Pass RH, Silver E, Sampson KJ, and Kass RS (2007). A novel and lethal de novo LQT-3 mutation in a newborn with distinct molecular pharmacology and therapeutic response. PLoS One 2, e1258. [PubMed: 18060054]

Baroudi G, Acharfi S, Larouche C, and Chahine M (2002). Expression and intracellular localization of an SCN5A double mutant R1232W/T1620M implicated in Brugada syndrome. Circ Res 90, E11–16. [PubMed: 11786529]

Baroudi G, Pouliot V, Denjoy I, Guicheney P, Shrier A, and Chahine M (2001). Novel mechanism for Brugada syndrome: defective surface localization of an SCN5A mutant (R1432G). Circ Res 88, E78–83. [PubMed: 11420310]

Bennett ES (2001). Channel cytoplasmic loops alter voltage-dependent sodium channel activation in an isoform-specific manner. J Physiol 535, 371–381. [PubMed: 11533130]

Bennett PB, Yazawa K, Makita N, and George AL Jr. (1995). Molecular mechanism for an inherited cardiac arrhythmia. Nature 376, 683–685. [PubMed: 7651517]

Capes DL, Goldschen-Ohm MP, Arcisio-Miranda M, Bezanilla F, and Chanda B (2013). Domain IV voltage-sensor movement is both sufficient and rate limiting for fast inactivation in sodium channels. J Gen Physiol 142, 101–112. [PubMed: 23858005]

Catterall WA (2000). From ionic currents to molecular mechanisms: The structure and function of voltage-gated sodium channels. Neuron 26, 13–25. [PubMed: 10798388]

Catterall WA, and Maier SKG (2015). Voltage-gated sodium channels and the electrical excitability of the heart. In Cardiac Electrophysiology: From Bench to Bedside, Zipes DJ, and Jalife J, eds. (Saunders/Elsevier).

Catterall WA, Wisedchaisri G, and Zheng N (2017). The chemical basis for electrical signaling. Nature Chem Biol 13, 455–463. [PubMed: 28406893]

Chakrabarti N, Ing C, Payandeh J, Zheng N, Catterall WA, and Pomes R (2013). Catalysis of Na^+ permeation in the bacterial sodium channel Na_VAb. Proc Natl Acad Sci U S A 110, 11331–11336. [PubMed: 23803856]

Chanda B, and Bezanilla F (2002). Tracking voltage-dependent conformational changes in skeletal muscle sodium channel during activation. J Gen Physiol 120, 629–645. [PubMed: 12407076]

DeCaen PG, Yarov-Yarovoy V, Scheuer T, and Catterall WA (2011). Gating charge interactions with the S1 segment during activation of a Na^+ channel voltage sensor. Proc Natl Acad Sci U S A 108, 18825–18830. [PubMed: 22042870]

DeCaen PG, Yarov-Yarovoy V, Sharp EM, Scheuer T, and Catterall WA (2009). Sequential formation of ion pairs during activation of a sodium channel voltage sensor. Proc Natl Acad Sci U S A 106, 22498–22503. [PubMed: 20007787]

DeCaen PG, Yarov-Yarovoy V, Zhao Y, Scheuer T, and Catterall WA (2008). Disulfide locking a sodium channel voltage sensor reveals ion pair formation during activation. Proc Natl Acad Sci U S A 105, 15142–15147. [PubMed: 18809926]

Dichgans M, Freilinger T, Eckstein G, Babini E, Lorenz-Depiereux B, Biskup S, Ferrari MD, Herzog J, van den Maagdenberg AM, Pusch Mv et al. (2005). Mutation in the neuronal voltage-gated

sodium channel SCN1A in familial hemiplegic migraine. Lancet 366, 371–377. [PubMed: 16054936]

Emsley P, Lohkamp B, Scott WG, and Cowtan K (2010). Features and development of Coot. Acta Crystallogr D Biol Crystallogr 66, 486–501. [PubMed: 20383002]

Favre I, Moczydlowski E, and Schild L (1996). On the structural basis for ionic selectivity among Na^+, K^+, and Ca^{2+} in the voltage-gated sodium channel. Biophys J 71, 3110–3125. [PubMed: 8968582]

Fozzard HA, and Hanck DA (1996). Structure and function of voltage-dependent sodium channels: Comparison of brain II and cardiac isoforms. Physiol Rev 76, 887–926. [PubMed: 8757791]

Gamal El-Din TM, Lenaeus MJ, Zheng N, and Catterall WA (2018). Fenestrations control resting-state block of a voltage-gated sodium channel. Proc Natl Acad Sci U S A 115, 13111–13116. [PubMed: 30518562]

Gamal El-Din TM, Scheuer T, and Catterall WA (2014). Tracking S4 movement by gating pore currents in the bacterial sodium channel NaChBac. J Gen Physiol 144, 147–157. [PubMed: 25070432]

Goehring A, Lee CH, Wang KH, Michel JC, Claxton DP, Baconguis I, Althoff T, Fischer S, Garcia KC, and Gouaux E (2014). Screening and large-scale expression of membrane proteins in mammalian cells for structural studies. Nat Protoc 9, 2574–2585. [PubMed: 25299155]

Goldin AL, Barchi RL, Caldwell JH, Hofmann F, Howe JR, Hunter JC, Kallen RG, Mandel G, Meisler MH, Berwald Netter Y, et al. (2000). Nomenclature of voltage-gated sodium channels. Neuron 28, 365–368. [PubMed: 11144347]

Goldschen-Ohm MP, Capes DL, Oelstrom KM, and Chanda B (2013). Multiple pore conformations driven by asynchronous movements of voltage sensors in a eukaryotic sodium channel. Nature communications 4, 1350.

Gordon D, Merrick D, Wollner DA, and Catterall WA (1988). Biochemical properties of sodium channels in a wide range of excitable tissues studied with site-directed antibodies. Biochemistry 27, 7032–7038. [PubMed: 2848576]

Grant T, Rohou A, and Grigorieff N (2018). cisTEM, user-friendly software for single-particle image processing. eLife 7.

Heinemann SH, Terlau H, Stuhmer W, Imoto K, and Numa S (1992). Calcium channel characteristics conferred on the sodium channel by single mutations. Nature 356, 441–443. [PubMed: 1313551]

Henderson R, Sali A, Baker ML, Carragher B, Devkota B, Downing KH, Egelman EH, Feng Z, Frank J, Grigorieff N, et al. (2012). Outcome of the first electron microscopy validation task force meeting. Structure 20, 205–214. [PubMed: 22325770]

Hille B (1971). The permeability of the sodium channel to organic cations in myelinated nerve. J Gen Physiol 59, 599–619.

Hille B (1972). The permeability of the sodium channel to metal cations in myelinated nerve. J Gen Physiol 59, 637–658. [PubMed: 5025743]

Hille B (1975a). Ionic selectivity, saturation, and block in sodium channels. A four-barrier model. J Gen Physiol 66, 535–560. [PubMed: 1194886]

Hille B (1975b). The receptor for tetrodotoxin and saxitoxin: a structural hypothesis. BiophysJ 15, 615–619. [PubMed: 1148362]

Isom DG, Castaneda CA, Cannon BR, and Garcia-Moreno B (2011). Large shifts in pKa values of lysine residues buried inside a protein. Proc Natl Acad Sci U S A 108, 5260–5265. [PubMed: 21389271]

Isom LL, De Jongh KS, and Catterall WA (1994). Auxiliary subunits of voltage-gated ion channels. Neuron 12, 1183–1194. [PubMed: 7516685]

Isom LL, Ragsdale DS, De Jongh KS, Westenbroek RE, Reber BF, Scheuer T, and Catterall WA (1995). Structure and function of the β2 subunit of brain sodium channels, a transmembrane glycoprotein with a CAM motif. Cell 83, 433–442. [PubMed: 8521473]

Jiang D, Gamal El-Din TM, Ing C, Lu P, Pomes R, Zheng N, and Catterall WA (2018). Structural basis for gating pore current in periodic paralysis. Nature 557, 590–594. [PubMed: 29769724]

Jurrus E, Engel D, Star K, Monson K, Brandi J, Felberg LE, Brookes DH, Wilson L, Chen J, Liles K, et al. (2018). Improvements to the APBS biomolecular solvation software suite. Protein Sci 27, 112–128. [PubMed: 28836357]

Kapplinger JD, Tester DJ, Alders M, Benito B, Berthet M, Brugada J, Brugada P, Fressart V, Guerchicoff A, Harris-Kerr C, et al. (2010). An international compendium of mutations in the SCN5A-encoded cardiac sodium channel in patients referred for Brugada syndrome genetic testing. Heart Rhythm 7, 33–46. [PubMed: 20129283]

Kawate T, and Gouaux E (2006). Fluorescence-detection size-exclusion chromatography for precrystallization screening of integral membrane proteins. Structure 14, 673–681. [PubMed: 16615909]

Kellenberger S, Scheuer T, and Catterall WA (1996). Movement of the Na^+ channel inactivation gate during inactivation. J Biol Chem 271, 30971–30979. [PubMed: 8940085]

Konzen G, Reichardt B, and Hauswirth O (1990). Fast and slow blockade of sodium channels by flecainide in rabbit cardiac Purkinje fibres. Naunyn Schmiedebergs ArchPharmacol 341, 565–576.

Li W, Yin L, Shen C, Hu K, Ge J, and Sun A (2018). SCN5A Variants: Association With Cardiac Disorders. Front Physiol 9, 1372. [PubMed: 30364184]

Liu H, Atkins J, and Kass RS (2003a). Common molecular determinants of flecainide and lidocaine block of heart Na^+ channels: evidence from experiments with neutral and quaternary flecainide analogues. J Gen Physiol 121, 199–214. [PubMed: 12601084]

Liu H, Clancy C, Cormier J, and Kass R (2003b). Mutations in cardiac sodium channels: clinical implications. Am J Pharmacogenomics 3, 173–179. [PubMed: 12814325]

Lombet A, and Lazdunski M (1984). Characterization, solubilization, affinity labeling, and purification of the cardiac sodium channel using Tityus toxin. Eur J Biochem 141, 651–660. [PubMed: 6086336]

Makita N, Bennett PB Jr., and George AL Jr. (1994). Voltage-gated Na^+ channel beta-1 subunit mRNA expressed in adult human skeletal muscle, heart, and brain is encoded by a single gene. J Biol Chem 269, 7571–7578. [PubMed: 8125980]

McPhee JC, Ragsdale D, Scheuer T, and Catterall WA (1998). A critical role for the S4-S5 intracellular loop in domain IV of the sodium channel alpha subunit in fast inactivation. J Biol Chem 273, 1121–1129. [PubMed: 9422778]

McPhee JC, Ragsdale DS, Scheuer T, and Catterall WA (1994). A mutation in segment IVS6 disrupts fast inactivation of sodium channels. Proc Natl Acad Sci U S A 91, 12346–12350. [PubMed: 7991630]

McPhee JC, Ragsdale DS, Scheuer T, and Catterall WA (1995). A critical role for transmembrane segment IVS6 of the sodium channel alpha subunit in fast inactivation. J Biol Chem 270, 12025–12034. [PubMed: 7744852]

Moreau A, and Chahine M (2018). A new cardiac channelopathy: from clinical phenotypes to molecular mechanisms associated with Nav1.5 gating pores. Front Cardiovasc Med 5, 139. [PubMed: 30356750]

Moreau A, Gosselin-Badaroudine P, Boutjdir M, and Chahine M (2015). Mutations in the voltage sensors of domains I and II of Nav1.5 that are associated with arrhythmias and dilated cardiomyopathy generate gating pore currents. Front Pharmacol 6, 301. [PubMed: 26733869]

Nguyen PT, DeMarco KR, Vorobyov I, Clancy CE, and Yarov-Yarovoy V (2019). Structural basis for antiarrhythmic drug interactions with the human cardiac sodium channel. Proc Natl Acad Sci U S A 116, 2945–2954. [PubMed: 30728299]

Noda M, Shimizu S, Tanabe T, Takai T, Kayano T, Ikeda T, Takahashi H, Nakayama H, Kanaoka Y, Minamino N, et al. (1984). Primary structure of Electrophorus electricus sodium channel deduced from cDNA sequence. Nature 312, 121–127. [PubMed: 6209577]

Noda M, Suzuki H, Numa S, and Stuhmer W (1989). A single point mutation confers tetrodotoxin and saxitoxin insensitivity on the sodium channel II. FEBS Lett 259, 213–216. [PubMed: 2557243]

Numa S, and Noda M (1986). Molecular structure of sodium channels. Ann N Y Acad Sci 479, 338–355. [PubMed: 2434000]

O'Malley HA, and Isom LL (2015). Sodium channel beta subunits: emerging targets in channelopathies. Annu Rev Physiol 77, 481–504. [PubMed: 25668026]

Pan X, Li Z, Huang X, Huang G, Gao S, Shen H, Liu L, Lei J, and Yan N (2019). Molecular basis for pore blockade of human Na^+ channel $Na_V1.2$ by the mu-conotoxin KIIIA. Science 363, 1309–1313. [PubMed: 30765605]

Pan X, Li Z, Zhou Q, Shen H, Wu K, Huang X, Chen J, Zhang J, Zhu X, Lei J, et al. (2018). Structure of the human voltage-gated sodium channel $Na_V1.4$ in complex with beta1. Science 362, pii: eaau2486. [PubMed: 30190309]

Payandeh J, Gamal El-Din TM, Scheuer T, Zheng N, and Catterall WA (2012). Crystal structure of a voltage-gated sodium channel in two potentially inactivated states. Nature 486 135–139. [PubMed: 22678296]

Payandeh J, Scheuer T, Zheng N, and Catterall WA (2011). The crystal structure of a voltage-gated sodium channel. Nature 475, 353–358. [PubMed: 21743477]

Pettersen EF, Goddard TD, Huang CC, Couch GS, Greenblatt DM, Meng EC, and Ferrin TE (2004). UCSF Chimera--a visualization system for exploratory research and analysis. Journal of computational chemistry 25, 1605–1612. [PubMed: 15264254]

Qu Y, Isom LL, Westenbroek RE, Rogers JC, Tanada TN, McCormick KA, Scheuer T, and Catterall WA (1995). Modulation of cardiac Na^+ channel expression in Xenopus oocytes by beta-1 subunits. J Biol Chem 270, 25696–25701. [PubMed: 7592748]

Ragsdale DS, McPhee JC, Scheuer T, and Catterall WA (1996). Common molecular determinants of local anesthetic, antiarrhythmic, and anticonvulsant block of voltage-gated Na^+ channels. Proc Natl Acad Sci U S A 93, 9270–9275. [PubMed: 8799190]

Reeves PJ, Callewaert N, Contreras R, and Khorana HG (2002). Structure and function in rhodopsin: high-level expression of rhodopsin with restricted and homogeneous N-glycosylation by a tetracycline-inducible N-acetylglucosaminyltransferase I-negative HEK293S stable mammalian cell line. Proc Natl Acad Sci U S A 99, 13419–13424. [PubMed: 12370423]

Ren D, Navarro B, Xu H, Yue L, Shi Q, and Clapham DE (2001). A prokaryotic voltage-gated sodium channel. Science 294, 2372–2375. [PubMed: 11743207]

Rogart RB, Cribbs LL, Muglia LK, Kephart DD, and Kaiser MW (1989). Molecular cloning of a putative tetrodotoxin-resistant rat heart Na^+ channel isoform. Proc Natl Acad Sci USA 86, 8170–8174. [PubMed: 2554302]

Rohl CA, Boeckman FA, Baker C, Scheuer T, Catterall WA, and Klevit RE (1999). Solution structure of the sodium channel inactivation gate. Biochemistry 38, 855–861. [PubMed: 9893979]

Sampson KJ, and Kass RK (2011). Antiarrhythmic Drugs. In Goodman & Gilman's Pharmacological Basis of Therapeutics, pp. 815–848.

Scheres SH (2012). RELION: implementation of a Bayesian approach to cryo-EM structure determination. J Struct Biol 180, 519–530. [PubMed: 23000701]

Shen H, Liu D, Wu K, Lei J, and Yan N (2019). Structures of human $Na_V1.7$ channel in complex with auxiliary subunits and animal toxins. Science.

Shen H, Zhou Q, Pan X, Li Z, Wu J, and Yan N (2017). Structure of a eukaryotic voltage-gated sodium channel at near-atomic resolution. Science, eaal4326. [PubMed: 28183995]

Sivilotti L, Okuse K, Akopian AN, Moss S, and Wood JN (1997). A single serine residue confers tetrodotoxin insensitivity on the rat sensory-neuron-specific sodium channel SNS. FEBS Lett 409, 49–52. [PubMed: 9199502]

Smith MR, and Goldin AL (1997). Interaction between the sodium channel inactivation linker and domain III S4-S5. BiophysJ 73, 1885–1895. [PubMed: 9336184]

Sokolov S, Scheuer T, and Catterall WA (2007). Gating pore current in an inherited ion channelopathy. Nature 446, 76–78. [PubMed: 17330043]

Sokolov S, Scheuer T, and Catterall WA (2008). Depolarization-activated gating pore current conducted by mutant sodium channels in potassium-sensitive normokalemic periodic paralysis. Proc Natl Acad Sci U S A 105, 19980–19985. [PubMed: 19052238]

Struyk AF, and Cannon SC (2007). A Na^+ channel mutation linked to hypokalemic periodic paralysis exposes a proton-selective gating pore. J Gen Physiol 130, 11–20. [PubMed: 17591984]

Suloway C, Pulokas J, Fellmann D, Cheng A, Guerra F, Quispe J, Stagg S, Potter CS, and Carragher B (2005). Automated molecular microscopy: the new Leginon system. J Struct Biol 151, 41–60. [PubMed: 15890530]

Sun YM, Favre I, Schild L, and Moczydlowski E (1997). On the structural basis for size-selective permeation of organic cations through the voltage-gated sodium channel - Effect of alanine

mutations at the DEKA locus on selectivity, inhibition by Ca^{2+} and H^{+}, and molecular sieving. J Gen Physiol 110, 693–715. [PubMed: 9382897]

Sunami A, Glaaser IW, and Fozzard HA (2000). A critical residue for isoform difference in tetrodotoxin affinity is a molecular determinant of the external access path for local anesthetics in the cardiac sodium channel. Proc Natl Acad Sci U S A 97, 2326–2331. [PubMed: 10681444]

Terlau H, Heinemann SH, Stuhmer W, Pusch M, Conti F, Imoto K, and Numa S (1991). Mapping the site of block by tetrodotoxin and saxitoxin of sodium channel II. FEBS Lett 293, 93–96. [PubMed: 1660007]

Vilas JL, Gomez-Blanco J, Conesa P, Melero R, Miguel de la Rosa-Trevin J, Oton J, Cuenca J, Marabini R, Carazo JM, Vargas J, et al. (2018). MonoRes: Automatic and accurate estimation of local resolution for electron microscopy maps. Structure 26, 337–344 e334. [PubMed: 29395788]

Walker JR, Novick PA, Parsons WH, McGregor M, Zablocki J, Pande VS, and Du Bois J (2012). Marked difference in saxitoxin and tetrodotoxin affinity for the human nociceptive voltage-gated sodium channel (NaV1.7) Proc Natl Acad Sci U S A 109, 18102–18107. [PubMed: 23077250]

Wang GK, Russell C, and Wang SY (2003). State-dependent block of wild-type and inactivation-deficient Na^{+} channels by flecainide. J Gen Physiol 122, 365–374. [PubMed: 12913091]

West JW, Patton DE, Scheuer T, Wang Y, Goldin AL, and Catterall WA (1992). A cluster of hydrophobic amino acid residues required for fast Na^{+} channel inactivation. Proc Natl Acad Sci U S A 89, 10910–10914. [PubMed: 1332060]

Wisedchaisri G, Tonggu L, McCord E, Gamal El-Din TM, Wang L, Zheng N, and Catterall WA (2019). Resting-state structure and gating mechanism of a voltage-gated sodium channel. Cell 178, 993–1003. [PubMed: 31353218]

Wu X, Lee J, and Brooks BR (2017). Origin of pKa Shifts of Internal Lysine Residues in SNase Studied Via Equal-Molar VMMS Simulations in Explicit Water. J Phys Chem B 121, 3318–3330. [PubMed: 27700118]

Yang N, George AL Jr., and Horn R (1996). Molecular basis of charge movement in voltage-gated sodium channels. Neuron 16, 113–122. [PubMed: 8562074]

Yang N, and Horn R (1995). Evidence for voltage-dependent S4 movement in sodium channels. Neuron 15, 213–218. [PubMed: 7619524]

Yarov-Yarovoy V, Decaen PG, Westenbroek RE, Pan CY, Scheuer T, Baker D, and Catterall WA (2012). Structural basis for gating charge movement in the voltage sensor of a sodium channel. Proc Natl Acad Sci USA 109 E93–E102. [PubMed: 22160714]

Zhang K (2016). Gctf: Real-time CTF determination and correction. J Struct Biol 193, 1–12. [PubMed: 26592709]

Zheng SQ, Palovcak E, Armache JP, Verba KA, Cheng Y, and Agard DA (2017). MotionCor2: anisotropic correction of beam-induced motion for improved cryo-electron microscopy. Nat Methods 14, 331–332. [PubMed: 28250466]

Highlights

- The structure of the cardiac sodium channel reveals key functional features
- The antiarrhythmic drug flecainide blocks the pore below the selectivity filter
- The ion selectivity filter and inactivation gate are revealed in atomic detail
- An arrhythmia mutation creates a pathogenic gating pore ~2Å in diameter

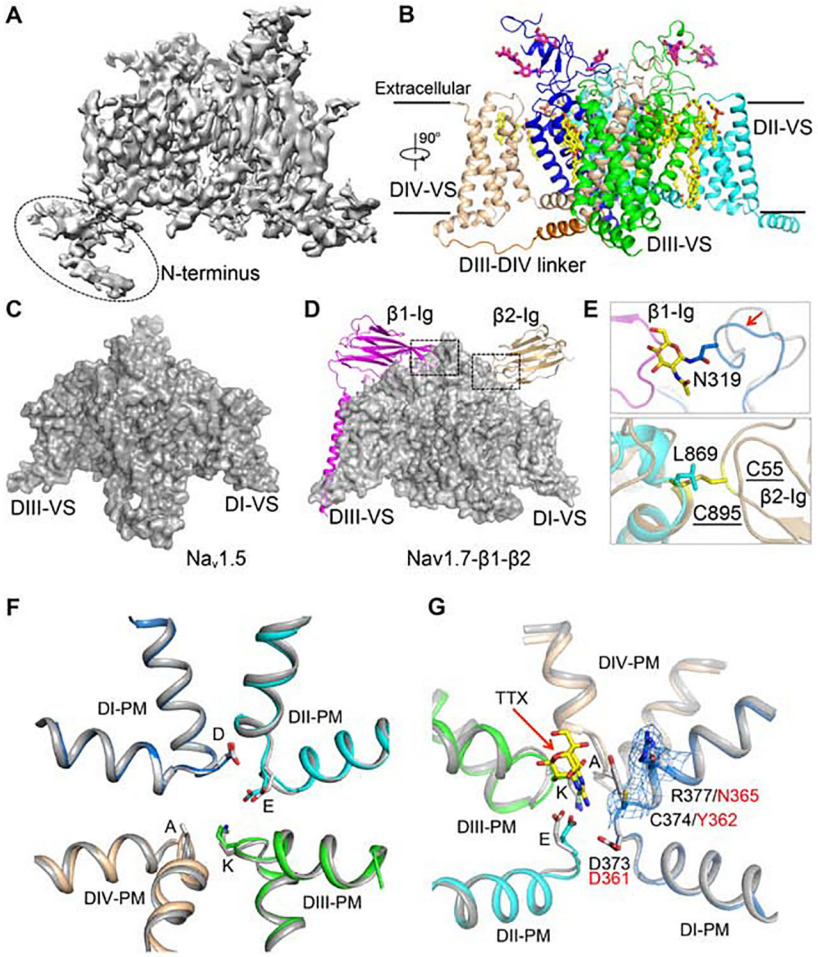

Figure 1. Cryo-EM Structure of rNa$_V$1.5$_C$

(A) Side view of the overall cryo-EM reconstruction of the rNa$_V$1.5$_C$.

(B) Cartoon representation of the overall structure of the rNa$_V$1.5$_C$. *D*I, *D*II, *D*III, *D*III-*D*IV linker, and *D*IV were colored blue, cyan, green, orange and wheat, respectively. The same color scheme is applied hereafter in this manuscript unless specified otherwise. The glycosyl moieties, lipids, and detergents shown in sticks are colored in magenta and yellow, respectively.

(C) Side view of rNa$_V$1.5$_C$ with surface colored in grey.

(D) Side view of human Na$_V$1.7-β1-β2 complex shown in grey surface for the α-subunit and in cartoons for β1 and β2 subunits colored in magenta and gold, respectively.

(E) Close-up view of β1 (Top panel) and β2 (Bottom panel) binding sites.

(F) SF alignment between rNa$_V$1.5$_C$ and Na$_V$1.7 (Grey). The side chains of the DEKA motif (DEKA: Asp373-Glu901-Lys1421-Ala1713) are shown in sticks.

(G) Comparison of the SF of the TTX-resistant rNa$_V$1.5$_c$ (colored) and the TTX-sensitive human Na$_V$1.7 (grey) with TTX bound. Cys374 and Arg377 are shown with electron density mesh presented at 3 a. TTX is shown in yellow. DEKA: Asp373-Glu901-Lys1421-Ala1713.

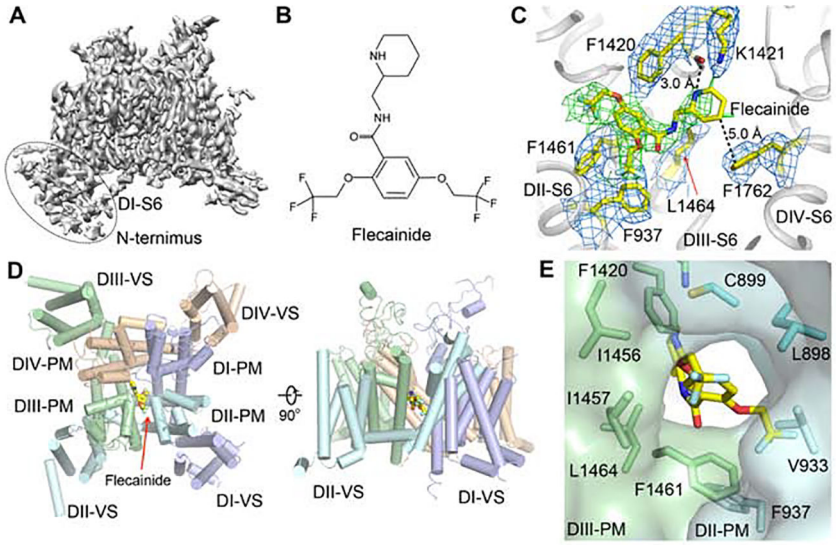

Figure 2. The Cryo-EM Structure of rNa$_V$1.5$_C$ and Flecainide Complex

(A) Side view of the overall cryo-EM reconstruction of the rNa$_V$1.5$_C$ and flecainide complex.

(B) Chemical structure of flecainide.

(C) EM density for flecainide binding pocket with key residues for flecainide binding shown in yellow sticks. The densities for the residues and flecainide were countered at 3 σ and colored in blue and green, respectively.

(D) Top and side view of rNa$_V$1.5$_C$ structure with flecainide shown in yellow sticks.

(E) Side view of *D*II-*D*III fenestration.

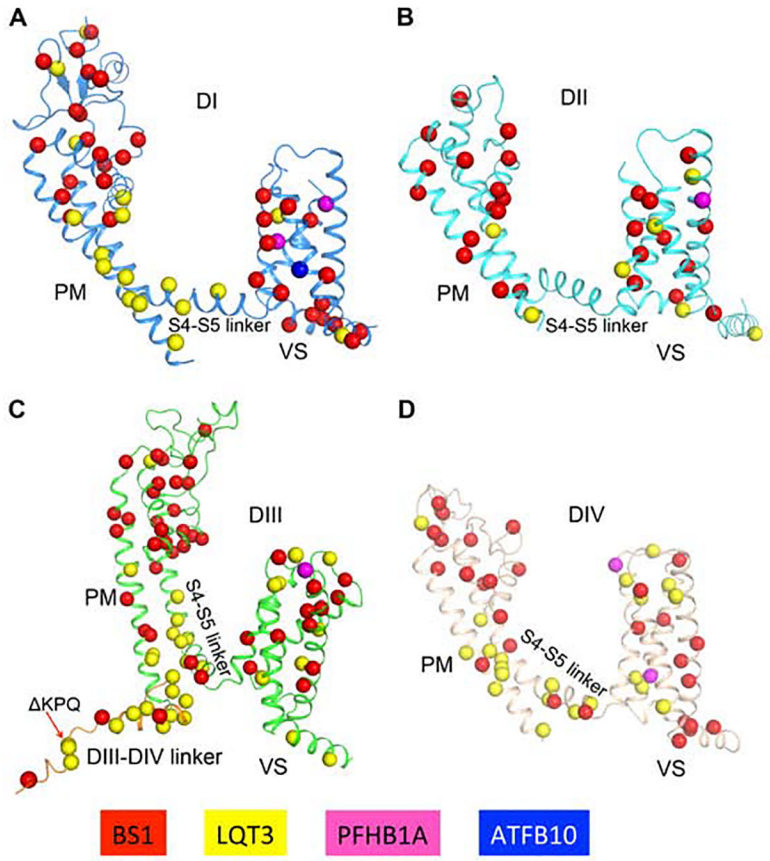

Figure 3. Molecular Mapping of Arrhythmia Mutations.

(A-D). Arrhythmia related mutations are located on *D*I, *D*II, *D*III and *D*IV. Mutation sites are shown in sticks for BS1, LQT3, PFHB1A and ATFB10 colored in red, yellow, magenta and blue, respectively.

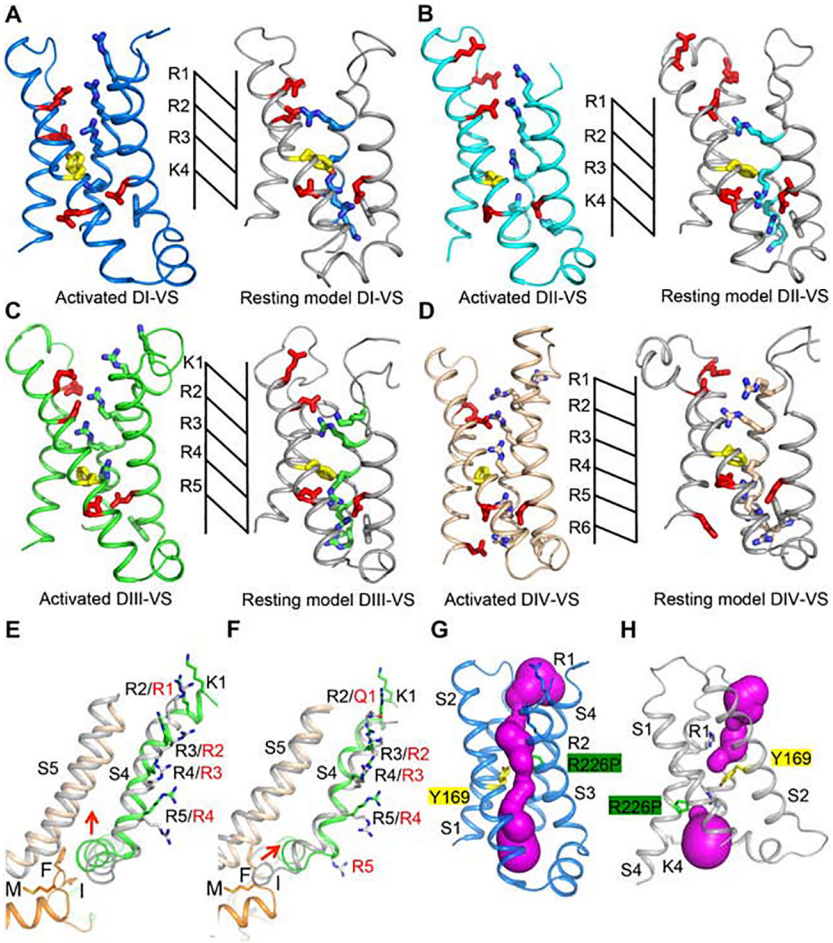

Figure 4. Structural Comparison of the DI-DIV VS in Activated and Resting States

(A-D) Structures of each of the four VS and the corresponding resting state models. Resting models are colored in grey. Key residues are shown with sidechains in sticks. Arg and Lys gating charges are colored blue, Glu residues in the ENC and INC are colored red, and the key Phe in the HCS is colored yellow. Extracellular Negative Cluster (ENC): *D*I, Asn145, Glu162; *D*II, Glu738, Glu747, Asn754; *D*III, Glu1227, Glu1242, Asp1245; *D*IV, Glu1550, Asp1556. Intracellular Negative Cluster (INC): *D*I, Glu172, Asp198; *D*II, Glu764, Asp786; *D*III, Glu1255, Asp1277; *D*IV, Asp1533, Glu1576, Asp1597.

(E) The VS of $rNa_V1.5_C$ *D*III aligned with the VS of the open-state structure of Na_vAb-Δ40 (PDB code: 5VB8) shown in grey.

(F) The VS of $rNa_V1.5_C$ DIII aligned with the VS of *D*III of Na_vPas in grey (PDB code: 6A90).

(G) Structure of the activated state of the VS of *D*I with the R226P mutation in green. Brugada Syndrome target residue Y169 is nearby in yellow. Water-accessible space calculated by MOLE2 is shown in magenta.

(H) Structure of the resting state of the VS of *D*I with the R226P mutation in green. Brugada Syndrome target residue Y169 is nearby in yellow. Water-accessible space calculated by MOLE2 is shown in magenta.

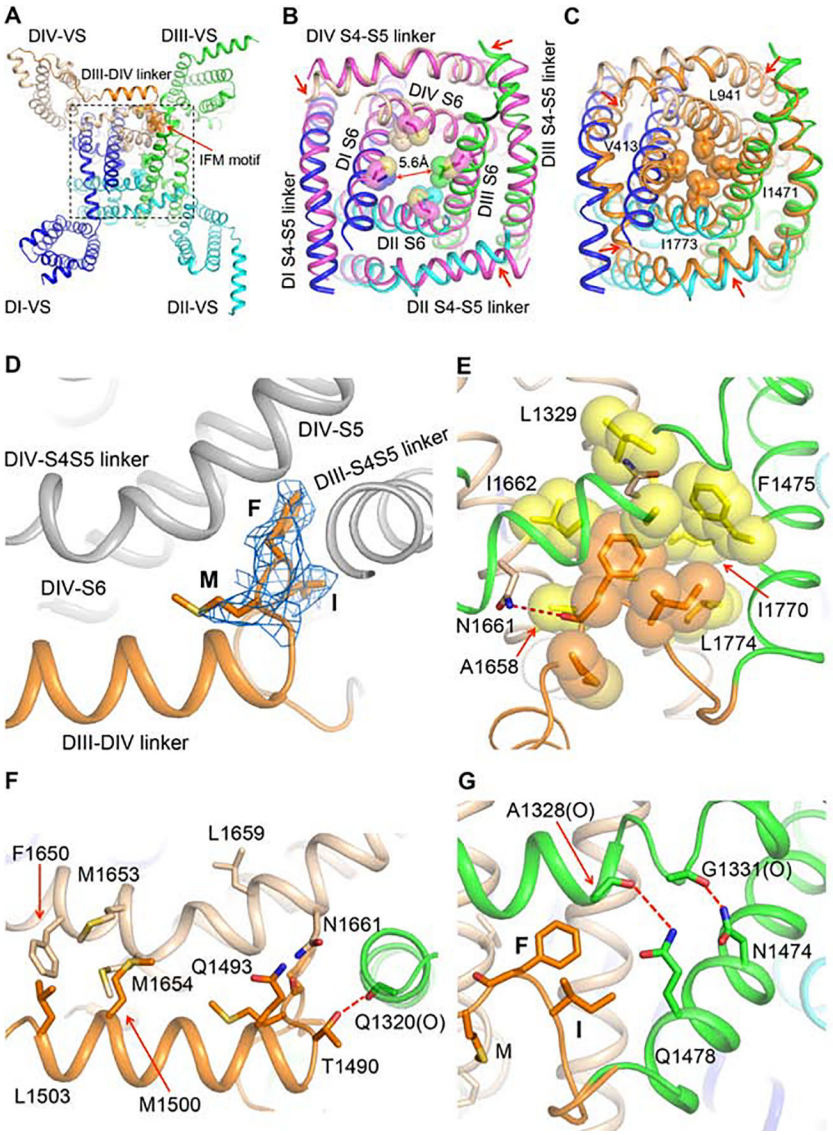

Figure 5. Activation and Fast Inactivation Gates.

(A) Bottom view of the rNa$_V$1.5$_C$ intracellular activation gate. The IFM motif (Ile1485-Phe1486-Met1487) and the sidechains of amino acid residues that partially close the activation gate are shown in sticks with half-transparent van der Waals surface.

(B) Close-up view of the rNa$_V$1.5$_C$ intracellular activation gate aligned with the open-state structure of Na$_V$Ab-Δ40 (PDB code: 5VB8) colored in magenta.

(C) Close-up view of the Na$_V$1.5$_C$ intracellular activation gate aligned with the resting state model of rNa$_V$1.5$_C$ activation gate calculated by MODELLER based on the resting state structure of Na$_V$Ab (PDB code: 6P6W). The resting model is colored in orange with key residues sealing the activation gate shown in sticks and half-transparent van der Waals surface.

(D) Side view of the IFM motif shown in sticks with electron density mesh contoured at 3 σ.

(E) Close-up view of IFM motif bound to the hydrophobic pocket shown in yellow. Dotted line in red, hydrogen bond.

(F) Interaction of *D*III-*D*IV linker with *D*III and *D*IV S4-S5 linker. “(O)” indicates an important interaction with a backbone carbonyl group. Dotted line in red, hydrogen bond. (G) Interaction of *D*III S6 with *D*III S4-S5 linker. “(O)” indicates an important interaction with a backbone carbonyl group. Dotted lines in red, hydrogen bonds.

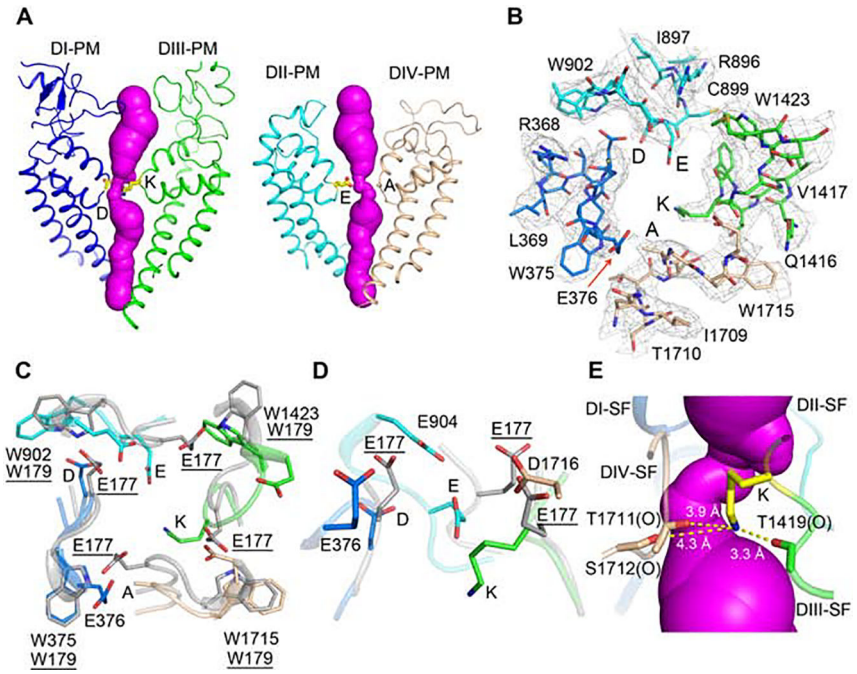

Figure 6. Structure of the Pore and the Ion Selectivity Filter.

(A) The open ion permeation path shown in magenta surface calculated by MOLE2. *D*I and *D*III PM with Asp373 and Lys1421 shown in sticks (Left panel), *D*II and *D*IV PM with Glu901 and Ala1713 shown in sticks (Right panel). DEKA: Asp373-Glu901-Lys1421-Ala1713.

(B) Top view of the $rNa_V1.5_C$ SF with electron density shown in grey mesh contoured at 3 σ.

(C) SF comparison of $Na_V1.5_c$ and activated Na_vAb (PDB,3RVY) shown in grey.

(D) Side view comparing the SF of $rNa_V1.5_c$ and activated Na_vAb (PDB,3RVY).

(E) The charge delocalization complex of Lys1421. Lys1421 side chain interacts with adjacent backbone carbonyl group of Thr1419, Thr1711 and Thr1712, which are indicated by “(O)”. Magenta surface represents the ion permeation pathway inside the SF.

Table 1.

Arrhythmia Mutations in the Conserved Transmembrane Domains

VS location	Position in $rNa_v1.5_c$	Human Mutation	Disease	Shift (Å)
DI-S3	A205	A204V	BS-1	5.8
DI-S4	T221	T220I	BS-1/SSS1	10.3
DI-S4	V224	V223L	BS-1	9.9
DI-S4	A227	A226V	BS-1	9.7
DI-S4	I231	I230V	BS-1	9.8
DI-S4	V233	V232I	BS-1	11.7
DI-S4	R223	R222Q	BS-1/LQT-3	9.9
DI-S4	R226	R225W	BS-1/LQT-3/PFHB1A	10.0
DII-S3	V790	V789I	BS-1	1.8
DII-S4	R809	R808P	BS-1	7.0
DII-S4	L813	L812Q	BS-1	6.1
DII-S4	R815	R814Q	BS-1	5.3
DII-S4	K818	K817E	BS-1	4.7
DII-S4	F817	F816Y	LQT-3	5.0
DIII-S3	L1285	L1283M	LQT-3	1.7
DIII-S4	T1306	T1304M	LQT-3	8.8
DIII-S4	L1313	L1311P	BS-1	6.9
DIV-S3	I1595	I1593M	LQT-3	1.7
DIV-S3	F1596	F1594S	LQT-3	1.2
DIV-S3	D1597	D1595N	PFHB1A	1.2
DIV-S3	V1606	V1604M	BS-1	1.8
DIV-S4	R1625	R1623Q	LQT-3/ BS-1	9.6
DIV-S4	R1628	R1626H/P	LQT-3	9.7
DIV-S4	R1631	R1629Q	BS-1	8.0

The human arrhythmia mutations located in each domain S3 and S4 of $rNa_V1.5_C$ are listed. Diseases caused by those mutations are indicated individually. The shift of each mutation represents the distance of Cα between $rNa_V1.5_C$ VS and the resting state model.